DEPARTMENT OF COMPUTER SCIENCE

THE GIMBALSCOPE: SPACECRAFT ATTITUDE CONTROL FOR HAPTIC FEEDBACK

A Parallel Dual Control Moment Gyroscope for Ungrounded Directional Force Feedback

Jordan Taylor

A dissertation submitted to the University of Bristol in accordance with the requirements of the degree of Master of Engineering in the Faculty of Engineering.

Tuesday 2nd May, 2023

Abstract

This dissertation details the design, development, and evaluation of the Gimbalscope: a wireless, ungrounded, three-degrees-of-freedom directional haptic feedback device.

The Gimbalscope utilises a scissored-pair Dual Control Moment Gyroscope with actuated gimbals to produce directional torque cues isolated to a single axis. The Gimbalscope is designed and manufactured using low-cost, open-standard components and software. Through doing this, I aim to make the production of gyroscopic haptic devices more accessible to researchers. I hypothesise that participants are able to correctly perceive the Gimbalscope's haptic torque cues and use the device as an orientation aid to correctly locate and identify target orientations.

0.1 Achievements

- I created a scissored-pair Dual Control Moment Gyroscope and used it to produce moments isolated to a single axis.
- I used the gyroscope to produce a remotely operated self-contained handheld haptic device.
- I evaluated the ability of users to perceive haptic cues about the *roll*, *pitch*, and *yaw* axes.
- I replicated the experimental findings of J M Walker's haptic DCMG device paper [34].
- I evaluated the ability of users to use the Gimbalscope to identify targets on the horizontal plane.

Dedication and Acknowledgements

I would like to express my appreciation for the Teaching Technologist Team at the University of Bristol, with particular note for the Hackspace. Although not having a direct influence in this Dissertation, I would not be equipped with the practical engineering skills I have today without the opportunity to learn-through-doing afforded by the team.

A massive thank you to my Mother, Father, and The Computer Science Year 4 Pastoral Tutor Chris Priest for supporting and enabling a part-time schedule of study as I deal with post-covid health issues.

Finally, an additional thanks to BIG (Bristol Interaction Group) for facilitating my work and being wonderful people.

Declaration

I declare that the work in this dissertation was carried out in accordance with the requirements of the University's Regulations and Code of Practice for Taught Programmes and that it has not been submitted for any other academic award. Except where indicated by specific reference in the text, this work is my own work. Work done in collaboration with, or with the assistance of others, is indicated as such. I have identified all material in this dissertation which is not my own work through appropriate referencing and acknowledgement. Where I have quoted or otherwise incorporated material which is the work of others, I have included the source in the references. Any views expressed in the dissertation, other than referenced material, are those of the author.

Jordan Taylor, Tuesday 2nd May, 2023

Contents

List of Figures

List of Tables

Ethics Statement

This project fits within the scope of ethics application 0026, as reviewed by my supervisor, Anne Roudaut.

Supporting Technologies

- A pair of standard 1806 2300Kv brushless motors were used to power the flywheels.
- A pair of 12V Micro Metal Geared Motors with Quadrature Encoders at 100:1 reduction were used to actuate the outer gimbals.
- A Bluebird BMS-620MG Metal Gear Analogue Servo was used for actuating the central gimbal.
- A pair of Adafruit RFM69HCW 900MHz Radio Transceivers and the RHRF69 radio driver library were used to wirelessly communicate with the Gimbalscope.
- A pair of Arduino Mega 2560 Rev3s were used to provide a platform for controlling the Gimbalscope and the PC communication dongle.
- An Arduino Micro was used as the Gimbalscope's dedicated radio transceiver operator.
- An Adafruit L3GD20H Triple-Axis Gyro Breakout Board was used with the Unified L3GD20 driver library for tracking the Gimbalscope's orientation.
- An MPU-6050 breakout board was used to provide a platform for vibration and gyroscopic force measurements.
- Microsoft 3D builder and Autodesk Fusion 360 were used to design the 3D printed parts used in creating the Gimbalscope.
- An Ultimaker 2 Extended+ 3D printer was used to fabricate structural components of the Gimbalscope.
- The Unity Real-Time Development Platform with the Ardity Arduino Serial Package was used to create bespoke Gimbalscope control software.
- The NumPy and matplotlib Python libraries were used to compute and plot results from user trials, as well as vibration and gyroscopic force data.

Notation and Acronyms

CMG	:	Control Moment Gyroscope
DCMG	:	Dual Control Moment Gyroscope
LED	:	Light Emitting Diode
RPM	:	Revolutions-Per-Minute
Kv	:	Estimation of RPM-per-Volt of a brushless motor in a no-load condition.
ESC	:	Electronic Speed Controller. Governs speed of a motor.
BEC	:	Battery Eliminator Circuit. Regulates voltage to connected circuit.
PWM	:	Pulse Width Modulation. Digital square wave with duty cycle.
PLA	:	Polylactic acid, a commonly used bioplastic 3D printer filament.
PID	:	Proportional-integral-derivative controller; a control loop mechanism.
IMU	:	Inertial Measurement Unit.
ISR	:	Interrupt Service Routine.
SDA	:	Serial Data.
SCL	:	Serial Clock.
I2C	:	Inter-Integrated Circuit. A synchronous multi-controller/multi-peripheral communication bus protocol.
UART	:	Universal Asynchronous Receiver / Transmitter
LiPo	:	Lithium Polymer Battery
CAD	:	Computer Aided Design
DC	:	Direct Current
EMF	:	Electromotive Force
MEMS	:	Microelectromechanical system
DOF	:	Degrees of Freedom
MOSFET	:	Metal–Oxide–Semiconductor Field-Effect Transistor

Chapter 1

Introduction

Haptic force feedback devices are designed to provide users with physical sensations in response to their interactions with a virtual environment. The main goals of haptic force feedback devices include enhancing the user's sense of immersion and realism, improving the user's performance and accuracy in tasks that require fine motor control, and affording a natural and intuitive user interface.

A key problem with current force feedback devices is balancing the three-way trade-off between form factor, workspace of interaction, and force fidelity. Designing a device with two of these tenets is difficult without sacrificing the third. In the hands of a user, the quality of a device can be evaluated as a function of all three. Conventional high-fidelity haptic feedback devices rely on transmitting ground-based reaction forces to the user via a series of rigid joints and links, restricting their portability. Contrastingly, ungrounded haptic feedback devices offer users kinesthetic or tactile feedback over a larger workspace. Many approaches to portable haptic feedback are designed to stimulate the skin through means such as vibration [21], skin deformation [29], or shape alteration [27] [28] [35]. These devices have many benefits such as their small size and light weight. According to Haptipdeia[24] - a database of haptic devices – there are few ungrounded handheld devices capable of directional force generation, and even fewer capable of inducing force in three degrees of freedom.

A solution is to use DCMGs (Dual Control Moment Gyroscopes). DCMGs are a form of gyroscope most commonly used in spacecraft attitude control systems [22]. They use a pair of counter-rotating flywheels to induce a torque about an axis. The majority of research carried out to produce haptic gyroscopic devices use expensive components, equipment, and bespoke machined parts, meaning that many of these devices are not reproducible.

This dissertation presents a prototype handheld DCMG-based haptic device named 'the Gimbalscope'. Truly ungrounded, remotely operated, and battery-powered, the Gimbalscope seeks to make a novel contribution to the field of ungrounded haptics and increase the accessibility of performing such research with its low-cost, open-standard components and open-source implementation. The Gimbalscope is evaluated in a variety of experiments designed to quantify the ability of humans to perceive torque generated from an ungrounded DCMG haptic feedback device. The device is shown in Figure 1.1.

1.1 Aims and Objectives

In the broadest sense, the aims and objectives of this dissertation are to:

1. Create a scissored-pair Dual Control Moment Gyroscope and use it to generate unambiguous torques.
2. Power the device from an internal power supply.
3. Wirelessly control the device from a computer.
4. Evaluate the ability of users to perceive a range of torques about different axes.
5. Evaluate the ability of users to use the Gimbalscope in real-world target identification scenarios.
6. Ensure open-source software and open-access components are used during development to make a contribution to the accessibility of research.

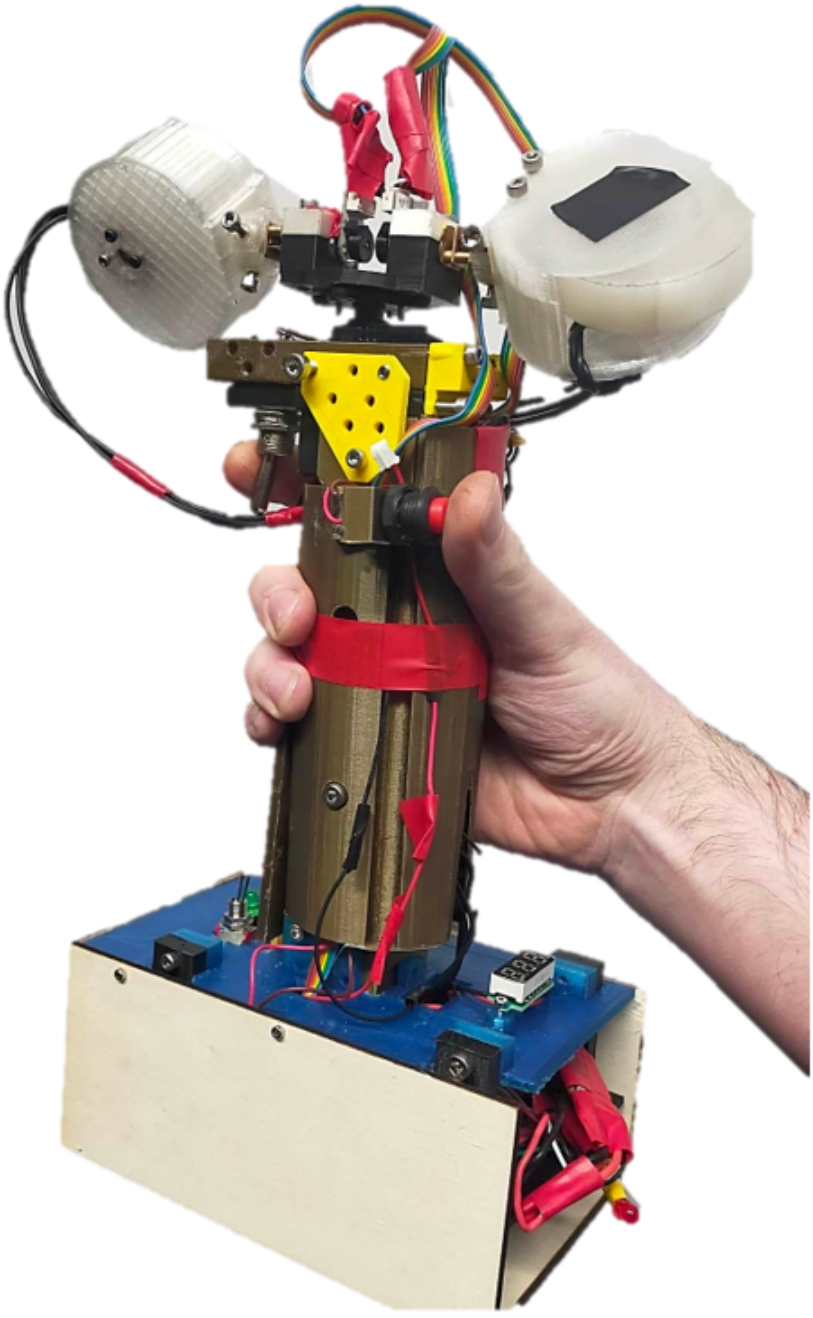

Figure 1.1: The final prototype of the Gimbalscope: an ungrounded and untethered DCMG-based directional haptic feedback device.

1.2 Gimbalscope Uses

An ungrounded DCMG-based haptic device has the potential to provide feedback for object interactions and guidance within virtual environments. Such a device could help with pointing or aiming adjustments in alignment tasks with a controlled torque. This could have a potential military application in investigating the effect of haptic cues on weapon aim, or have a place in sports science studying racquet sports. Furthermore, it could enable portable guidance through large environments. This could prove useful in disability studies investigating pedestrian navigation, providing a different sensory modality from sight and sound.

1.3 Report Structure

The content of this report is divided into six chapters. Related work in ungrounded haptic feedback is described in Chapter 2, providing an introduction to gyroscopic systems, as well as a relevant mathematical background.

Project execution is split across two chapters. Chapter 3 contains a technical breakdown and covers design decisions during development. Chapter 4 describes the motivations and experimental design of user testing.

A critical evaluation is given in Chapter 5 and is divided into three sections. It details technical and user-based evaluations of the Gimbalscope before evaluating important miscellaneous features.

A conclusion and ideas for further work are given in Chapter 6.

Chapter 2

Background

2.1 Related Work

2.1.1 Classifying Haptic Force Feedback Devices

For a human to experience mechanical influence from a haptic device it must impart a force or torque on the user. Newton's 3rd law states that forces always occur in equal and opposite pairs. Keeping this in mind, one may classify haptic interfaces into three categories based on their mechanical grounding configuration [8].

A classically grounded device rests on a table, floor, or another static object that can be used as leverage. They are made of mechanical linkages with rotational and translational joints. These devices employ actuators or brakes to create forces and torques between the user and the grounding element and are capable of producing high-fidelity feedback. An example is the statically mounted variant of Mantis [11]. Grounded devices are well represented in the commercial market, with particular prevalence in teleoperation with medical robotics and in nuclear fuel handling [26] [14]. However, grounded haptic devices suffer from finite workspace constraints and are costly solutions for large operational areas [31].

Body-grounded systems account for the second major category of haptic devices. Such devices are mounted to the user directly and use their fixture as a point of leverage for applying mechanical forces to parts of the wearer's body. Precise positioning and distribution of mounts and grounding forces can induce the perception of directed forces, despite each reaction being a zero-sum Newton pair [16]. Force fidelity and resolution are likely to be reduced in wearable systems compared to static mounts [16] [15]. Accessibility concerns pose design challenges in optimising device weight, strength, and ergonomics.

The haptic devices in the third category are not mechanically grounded and utilise linear or angular momentum to create sensations of force. They are not required to be mounted to a table or a person's body to produce the desired interaction forces, thus making them highly portable. Researchers have explored novel techniques for generating ungrounded directed force feedback, such as using jets of air [12] or utilising asymmetric oscillation [5] [23]. These methods are relatively energy inefficient as they either move a large amount of air or constantly add energy to a degrading mechanical system. As such, these are typically tethered to a static power supply to avoid the size and weight of onboard batteries. However, the idea of using gyroscopes to generate torque in ungrounded haptic feedback devices remains relatively unexplored [24].

2.1.2 Introduction to Mechanical Gyroscopes

Before critically evaluating related work, it is important to briefly introduce relevant gyroscopic mechanisms. An extended technical background is given in 2.2.

This dissertation concerns **mechanical** gyroscopes, i.e. those that consist of a spinning rotor mounted on a set of gimbals. The rotor maintains its axis of rotation due to the principle of angular momentum; *'a rotating object will maintain its axis of rotation in the absence of an external torque'*. Turning a rotor about an axis separate from that of its rotation results in an orthogonal torque. This is known as torque-induced precession.

Mechanical gyroscopes are commonly used in spacecraft attitude control - the process of controlling the orientation of a body with respect to an inertial frame of reference [22]. Attitude control can be achieved using various methods, including external thrusters, solar sails, and magnetic torquers - but most pertinently to this project, reaction wheels and Control Moment Gyroscopes (CMGs).

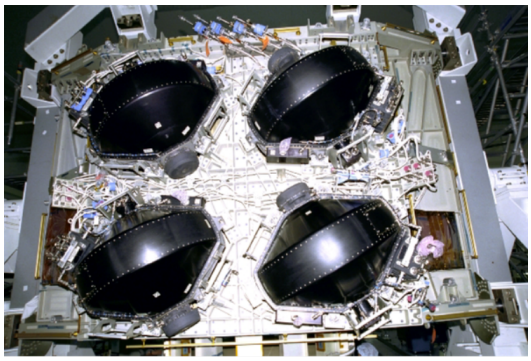

Figure 2.1: A Dual Control-Moment-Gyroscope used to orientate the International Space Station [13]

Reaction wheels

Reaction wheels consist of a motorised flywheel spinning on an axis. In the context of a stabilisation system, when turned about this axis, the flywheel experiences torque-induced precession. This causes the system to generate an equal and opposite moment perpendicular to the flywheel's axis of spin. The magnitude of the moment is proportional to the flywheel's angular deceleration. This keeps the gyroscope on a steady heading relative to an axis.

It is possible to generate a torque about the axis of rotation by spinning the flywheel up or down. This is how reaction wheels function. Reaction wheels are generally simpler in their design and operation than CMGs, so tend to be more reliable. [32].

Reaction wheels possess several drawbacks. When the speed of the flywheel fully saturates, it is no longer possible to induce a torque about at least one of the roll, pitch, and yaw axes. Reaction wheels must be mounted along three orthogonal axes to achieve three degrees of freedom of torque generation. They require large accelerations, heavy flywheels, and powerful motor brakes to produce substantial torque.

Control Moment Gyroscopes

In contrast to reaction wheels, Control Moment Gyroscopes consist of a spinning rotor and one or more motorised gimbals. The difference between reaction wheels and CMGs is that while the former applies torque through changes in its angular momentum, the latter alters the **axis** of the rotor's angular momentum without changing its speed.

When a gimbal motor changes the axis of the rotor's rotation, the induced torque is due to a constraint. As a result, the rotor itself does no mechanical work. Consequently, CMGs are more power efficient for exerting torque than reaction wheels. Mounting a flywheel on two perpendicular gimbals allows it to rotate through multiple axes, thus allowing for torque to be generated in any direction.

Despite these advantages, CMGs and reaction wheels share some common problems. One of the requirements of an ungrounded haptic feedback device is its ability to demonstrate transparency, which refers to generating minimal unwanted forces and torques as the user moves the device through free space.

Due to the effect of gravity, without spatial orientation resolution (keeping the axis of spin consistent with respect to the world), the rotor experiences a range of torques as it is moved and rotated. This results in a loss of transparency and is not ideal in a haptic feedback device. As a result, CMGs must be oriented relative to the ground to steer the rotor in opposing directions to counteract extraneous torques [17].

Dual Control Moment Gyroscopes

A solution to the problem of extraneous torque in CMG systems is to add a second rotor on its own set of gimbals, thus creating a Dual Control Moment Gyroscope (DCMG). With two rotors of equal angular momentum moving in parallel, it is possible to cancel the components of a moment about all but a single axis [33]. When the gimbals are stationary, a DCMG has zero resultant angular momentum, removing the problem of unwanted torque and the need for ground orientation tracking as seen in single CMG systems, producing a transparent device [33] [34].

The International Space Station uses a large DCMG array to maintain its orientation relative to Earth [13].

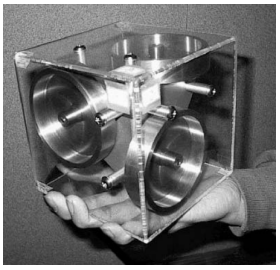

Figure 2.2: GyroCube

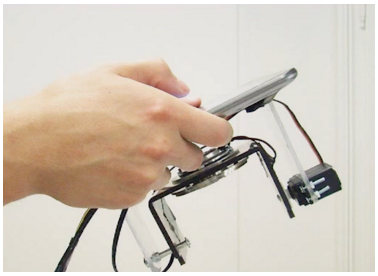

Figure 2.3: TorqueScreen

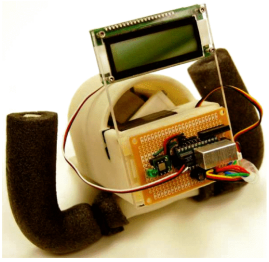

Figure 2.4: iTorqU 1.0

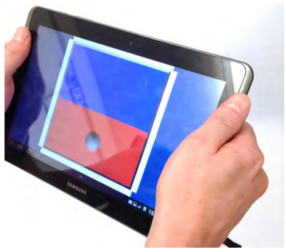

Figure 2.5: TorqueScreen Ball Balancing Exercise

Figure 2.6: iTorqU 2.0

2.1.3 Existing Handheld Gyroscopic Haptic Devices

This dissertation explores the potential of using a DCMG as the basis for a directional haptic feedback device. I have reviewed a set of existing devices to understand the advantages of such a setup. Each example described below encompasses the moment-generating capabilities of the previously described device.

The Gyrocube

Figure 2.2 shows the Gyrocube: an example of a three fixed-axis reaction wheel setup [32]. It features orthogonal flywheels in three axes that can be positively or negatively accelerated to generate torques with three degrees of freedom. The authors found that users encountered difficulties discerning the direction of produced torques due to unintended gyroscopic effects. Since all three wheels were spinning, when the angular momentum of one was changed, the other two acted as steered momentum wheels. This created unintended moments interfering with the intended resultant torque.

The TorqueScreen

The device shown in Figure 2.3 is the TorqueScreen [20]. The TorqueScreen consists of a single-axis CMG attached to the rear of a tablet. Its design expands on the prior work of the reaction wheel based GyroTab [7]. By using a CMG, unlike GyroCube and Gyrotab, TorqueScreen can provide consistent *active* torque-feedback, i.e., a haptic effect that can be dynamically controlled by the interactive system on demand.

The TorqueScreen aims to create external representations of digital interactions in accordance with *embodied cognition* [30], capitalising on human skills gained from prior experiences with objects in the real world. This is evident in Figure 2.5 with the TorqueScreen's ball balancing exercise.

Despite its vital contributions in demonstrating Jelle van Dijk et al.'s concept of *'sensorimotor coupling'* [30], the TorqueScreen possesses several mechanical shortcomings in its design. Limiting the design to a single flywheel and axis restricts the torque feedback to a single degree of freedom and imposes unwanted reactive torque as the tablet is rotated (as described in section 2.1.2).

The iTorqU 1.0

The iTorqU 1.0 shown in Figure 2.4 shares the same mechanical basis as the TorqueScreen and is designed to embody a two-handed steering wheel. Although a mechanical success, users reported that the unit was relatively heavy relative to its discernable output torque.

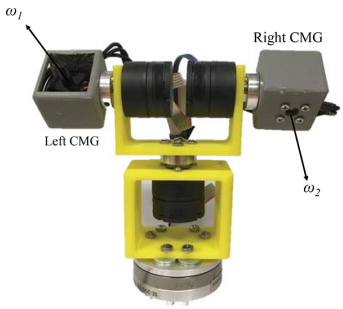

Figure 2.7: JM Walker's three-axis Haptic Scissored DCMG Device. [34]

The iTorqU 1.0's gimbal design restricted the rotor diameter, resulting in an unfavourable mass-to-moment-of-inertia ratio. Furthermore, the bandwidth of the gimbal actuator was insufficient to generate the desired range of output torques, restricting the device's range of motion. The actuator had a high level of friction, making self-stabilisation and transparency challenging to achieve. It was designed with a hobby-grade brushless motor to power the flywheel. While this meant it was capable of high-speed operation, the motor produced noticeable high-frequency vibrations when loaded with a heavy rotor. This was found to be a common issue amongst brushless hobby motors [17].

The iTorqU 2.0 and 2.1

Figure 2.6 shows the iTorqU 2.0; a two-axis, Three-Degrees-Of-Freedom CMG haptic device [17]. The device features a steel rotor CMG mounted atop a tennis racquet handle, affording familiar ergonomics. Its single-handed configuration was chosen to make torques more noticeable to the user. A separate MEMS gyroscope was used to inform the CMG's orientation to help achieve transparency. Torque is generated by quickly rotating the flywheel about an axis and slowly resetting it, resulting in apparent 'pulses' in a direction. The rate and size of these pulses were limited in the iTorqU 2.0 due to insufficiently powerful gimbal motors. This was rectified in version 2.1 [18].

J M Walker's DCMG Device

Figure 2.7 shows an example of a haptic scissored-pair DCMG device. A scissored-pair setup describes how the two flywheel gimbals rotate at equal and opposite angular velocities, crossing a common axis at the midpoints of their movements to create an isolated torque. Similarly to the iTorqU 2.0, this device delivers short moment pulses to invoke directional torque. However, adding a second contra-rotating flywheel eliminates undesired torques as the device moves through space. The rotation range of each gimbal is limited only by the wires supplying power to the flywheels' motors.

Walker's findings show that humans can unambiguously perceive 50Nmm moment cues generated by her DCMG device directions with a 99.3% success rate [34]. This improves upon the 70% identification rate of the 50 to 70 Nmm cues generated by the reaction-wheel-based GyroCube [32] as well as the 80% rate of 60Nmm cues generated by a single-CMG device [6].

2.1.4 Research Opportunity

The advantages of DCMG-based haptic devices should be evident after reviewing the previous sections 2.1.2 and 2.1.3. Unambiguous torques, self-stabilisation, low power consumption, and 3-DOF all contribute to a robust and transparent device. As such, the Gimbalscope builds upon the design of J M Walker's device *(Figure 2.7)* and feature a Dual-Control-Moment-Gyroscope.

Despite being ungrounded, none of the devices described in the section 2.1.3 are *untethered*. Each device is externally powered and relies on being physically connected to a computer for its control signals. As such, there is a novel contribution to be made in designing and evaluating a wireless, battery-powered, haptic DCMG device.

The cost of producing the Gimbalscope must be low, and the parts should be readily available. It is not accessible to produce the devices reviewed in the previous section without a substantial budget and facilities. For example, Walker's device utilises three Faulhaber Flat DC Micromotors with integrated encoders for its gimbal actuators which currently retail for approximately £100 each[2].

Furthermore, the performance characteristics of the Gimbalscope should be assessed using low-cost, readily available components. For an example of this necessity, the iTorqU 2.0's calibration tests were performed using an AMTI HE6X6–10-5 6-DOF grounded force/torque plate, a device unavailable to the public.

To further increase the accessibility of reproduction, the body of the Gimbalscope shall be 3D printed using PLA and assembled using standard metric nuts and bolts. The CAD files, circuit diagrams, and source code shall be freely available.

2.2 Technical Background

2.2.1 Mathematical Background

To quantify the torque generated by the Gimbalscope, it is necessary to provide a brief mathematical background on Control Moment Gyroscopes. It is crucial to show how it is possible to isolate a moment to a single axis. The following section shows how we derive the torque of a scissored-pair DCMG with a fixed central gimbal. This is demonstrated by working towards the general expression for a two-axis DCMG, before simplifying the expression to describe the fixed-gimbal-during-motion setup used by the Gimbalscope.

Using scalar notation, the angular momentum of a uniformly dense spinning flywheel F of mass m_F, radius r, and rotational frequency f may be given by:

$$L = \pi m_F f r^2 \tag{1}$$

However, we are working with vectors with respect to a Newtonian reference frame N. As such, angular velocity ω of a spinning flywheel F may be defined using rotational frequency if the direction of spin is known:

$$^N\vec{\omega}^F = 2\pi f, \tag{2}$$

Angular momentum L may more accurately be notated as $^N\vec{L}^{F/O}$ to represent the existence of reference frame N and an origin O. This requires defining the dyadic product of the flywheel's inertia $\vec{\vec{I}}^{F/F_{com}}$ where F_{com} is the centre of mass of flywheel F.

$$^N\vec{L}^{F/O} = \vec{\vec{I}}^{F/F_{com}} \cdot {}^N\vec{\omega}^F = L \tag{3}$$

Altering the direction or magnitude of flywheel F yields a torque $^N\vec{T}^{F/O}$. If the central point of the torque remains stationary throughout the motion, the resultant torque is given by the rate of change of angular momentum:

$$^N\vec{T}^{F/O} = {}^N\vec{L}^{F/O}\frac{d}{dt} \tag{4}$$

If we spin flywheel F and rotate its gimbal by an angle θ across any two orthogonal axes, a resultant torque is summoned in the third. Describing this requires considering the possibility of the flywheel centre of mass F_{com} moving through the space of N. This involves redefining angular momentum $^N\vec{L}^{F/O}$ as well as introducing the flywheel's potential translational velocity $^N\vec{v}^{F_{com}}$ as a factor. Angular momentum is given in equation 5, and resultant torque is given in equation 6 in its differentiated form.

$$^N\vec{L}^{F/O} = \vec{\vec{I}}^{F/F_{com}} \cdot {}^N\vec{\omega}^F + m_F\ {}^N\vec{v}^{F_{com}} \tag{5}$$

$$^N\vec{T}^{F/O} = \vec{\vec{I}}^{F/F_{com}} \cdot\ {}^N\vec{\alpha}^F + {}^N\vec{\omega}^F \times (\vec{\vec{I}}^{F/F_{com}} \cdot {}^N\vec{\omega}^F) + m_F\ r \times {}^N\vec{\alpha}^{F_{com}} \tag{6}$$

Where $^N\vec{\alpha}^F$ is the angular acceleration experienced by the flywheel in N from the perspective of a projection in a single axis, whereas $^N\vec{a}^{F_{com}}$ is the flywheel's translational acceleration in N. To simplify this expression, we shall assume that the flywheel has a constant scalar rotational frequency f and the gimbals have negligible inertia. Disabling one of the gimbals and locking its rotation allows us to look at a case where the orientation of the flywheel only changes in a single axis. As such, we may assume the flywheel's x and y orientation to be constant. This lets us remove the dyadic term $\vec{\vec{I}}^{F/F_{com}}$ and re-express $^N\vec{T}^{F/O}$ as the sum of the radial and axial moments of inertia I_{xx} and I_{zz} respectively.

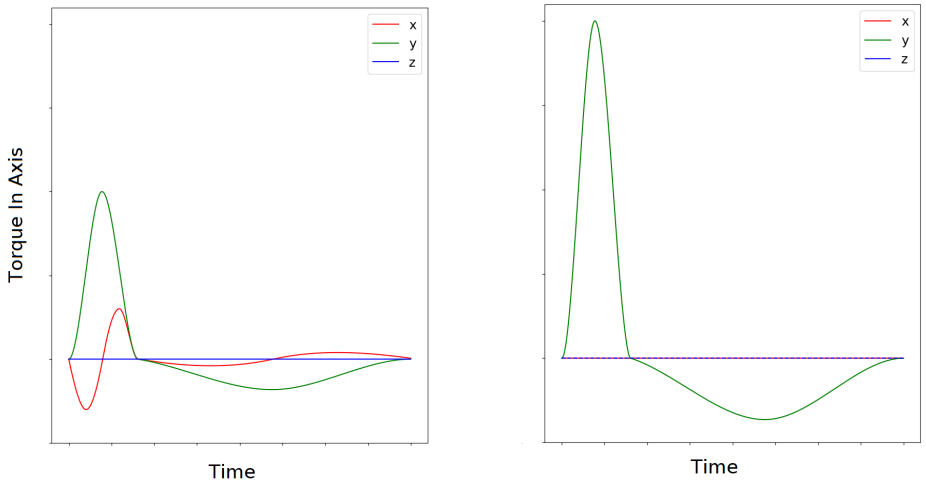

(a) Single CMG (b) Scissored-pair DCMG

Figure 2.8: Sketches of the moments generated by a CMG and DCMG rotating forward and slowly backwards on a single gimbal through angles $-\theta$ to θ.

$$^{N}\vec{T}^{F} = I_{xx}\dot{\phi}\ x - I_{zz}\phi\omega\cos(\theta)\ y - I_{zz}\phi\omega\sin(\theta)\ \hat{z} \tag{7}$$

Where ϕ denotes the angular velocity of the active gimbal and $\hat{z}$ describes the current z component of the flywheel's orientation.

Given that the gimbal rotates the flywheel about the x axis through $-\theta$ to θ, the resultant net torque would only be about the y axis. However, it is worth noting that this is the **resultant** torque, and applies only when each instantaneous torque component is integrated over the course of the movement.

Equation 7 contains terms for a z component of a moment. When evaluating the torque vector at almost any time throughout the motion, the unwanted z component is evident. As shown by the sketch in Subfigure 2.8a, the component oscillates in its direction as the gimbal moves and is the cause of transparency-reducing unwanted torques inherent in CMGs as discussed in Section 2.1.2.

It is possible to eliminate the effect of undesired torque components by introducing a second gyroscope and creating a DCMG. A second flywheel is spun in the opposite direction and rotated through a reverse trajectory of the first flywheel. This causes each CMG to create a positive torque in the y direction, while the second CMG generates torque components around the x and z axes equal and opposite to those produced by the first CMG. When both flywheels have identical moments of inertia, the orthogonal components will cancel out completely. This can be seen in Subfigure 2.8b. As such, assuming constant flywheel speeds ω, we may define the instantaneous torque vector of a DCMG as:

$$^{N}\vec{T}^{F/O} = -2I_{zz}\ \phi\ \omega\cos(\theta) \tag{8}$$

The absence of unwanted components enables a scissored-pair DCMG to attain greater angles of rotation and higher speeds, resulting in powerful moments around a single axis. Moreover, since the two flywheels are rotating in opposite directions, the overall angular momentum of the system is zero when the gimbals are stationary. As a result, the device does not oppose external rotations of the entire system, unlike reaction wheels and single CMGs. This would afford a haptic device full transparency.

2.2.2 PID Controllers

Proportional-Integral-Derivative (PID) systems are a widely used control mechanism in engineering. A PID controller is designed to continuously adjust the output of a system based on feedback from its inputs, ensuring that the system remains stable and responsive to changes in its environment.

The Proportional component of the PID controller provides a direct response to the difference between the target and the current value of a process variable. For example, the target versus current angular

velocity of a gimbal motor. This response is proportional to the magnitude of an error signal, resulting in a greater correction for greater errors.

The Integral component of the controller accumulates an error signal over time and adjusts the output accordingly. This helps to eliminate any steady-state error that may exist in the system.

The Derivative component of the controller predicts the system's future behaviour by analysing the rate of change of an error signal.

Often, controllers are designed using only two components of a PID system, referred to as either PI or PD controllers, including either integral or differential control components, respectively.

Compared to other control methods, PID systems are simple, robust, and versatile. They can be implemented using analogue and digital technology. However, the design of a PID system requires careful tuning of the controller parameters to ensure optimal performance. This involves adjusting the proportional, integral, and derivative gains to achieve the desired response characteristics.

2.2.3 Quadrature Encoders

Quadrature encoders are devices fitted to the shafts of motors which, when used in conjunction with a microcontroller, allow for real-time reading of the motor's orientation. Quadrature encoders function by generating two digital signals, A and B, which are 90 degrees out of phase as the motor shaft rotates. Knowing the state of A and B makes it possible to logically deduce the direction the motor shaft is spinning. It is usually necessary for these state updates to trigger an interrupt on the microcontroller.

2.2.4 Brushless motors and ESCs

Brushless motors require dedicated motor controllers because they operate differently from traditional DC motors. In a traditional DC motor, a commutator and brushes alternate a current to rotor coils, which generate a magnetic field that produces torque. However, brushless motors require three-phase power, which demands a polyphase alternating current. Brushless ESCs (electronic speed controllers) manage this process [25].

Brushless motors have a higher power-to-size ratio than brushed motors, making them more suitable for driving flywheels in a CMG device. Furthermore, brushless motors are generally more efficient than brushed motors due to their use of electronic commutation instead of mechanical commutation. As a result, they generate less heat and friction, which improves overall efficiency. This is important for battery-powered devices.

2.2.5 Lithium Polymer (LiPo) Batteries

Lithium Polymer batteries are a type of rechargeable battery known for their high energy density and high discharge characteristics. This makes them an ideal candidate for powering the Gimbalscope.

Despite their advantages, LiPo batteries are potentially dangerous if not handled properly. They can catch fire or explode if overcharged, punctured, or damaged. In such a situation, the smoke released is toxic and carcinogenic [19]. Less dangerously, LiPo batteries experience voltage drop as they are discharged and as such, deliver less power to a circuit as their charge depletes. This drop is proportional to the number of cells there are in the battery.

Chapter 3

Gimbalscope Design and Implementation

This chapter encompasses the design and workings of the Gimbalscope, as well as exploring the design decisions I made during the development process.

To summarise what has been learned in Chapter 2, the Gimbalscope is to fulfil the following requirements:

1. The device **must** be able to be held in a single hand, regardless of the user's handedness.
2. The device **must** be untethered, requiring no external physical connections between itself and a controller or power supply.
3. The device **must** be controllable in real-time.
4. The device **must** produce unambiguous torque output with no undesired components outside its intended torque axis.
5. The device **must** be transparent to the user, generating no undesired torques as it is moved and rotated through space.
6. The device **must** be developed and evaluated with free-to-use, open-source software.
7. The device **must** be constructed using readily available, open-standard and open-source components.
8. The device **must** have its schematics freely accessible to allow for its reproduction.
9. The device **must** be safe to operate.
10. The device **should** resemble an object familiar to most users, affording intuitive use.

The above points are referenced when a requirement is fulfilled throughout this chapter, indicated using angle brackets: e.g. ⟨req 1⟩.

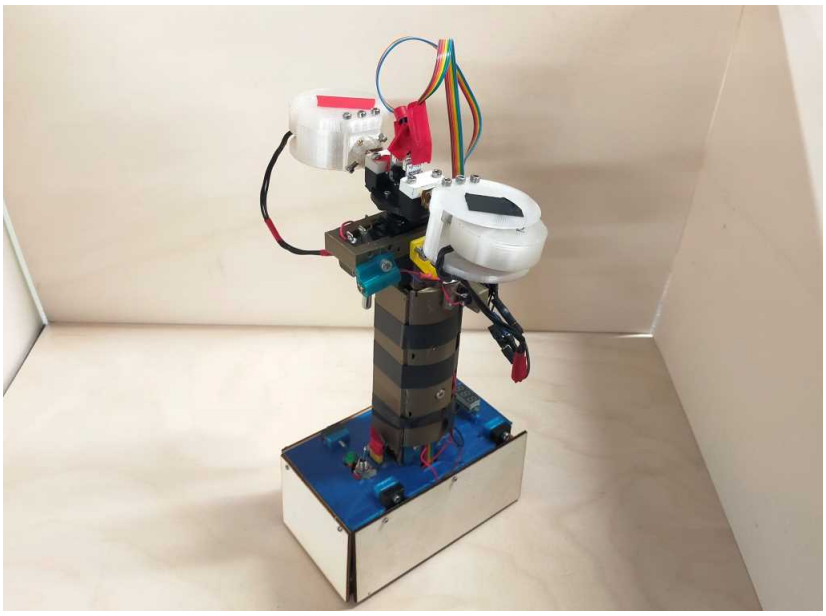

Figure 3.1: The Final Prototype of the Gimbalscope.

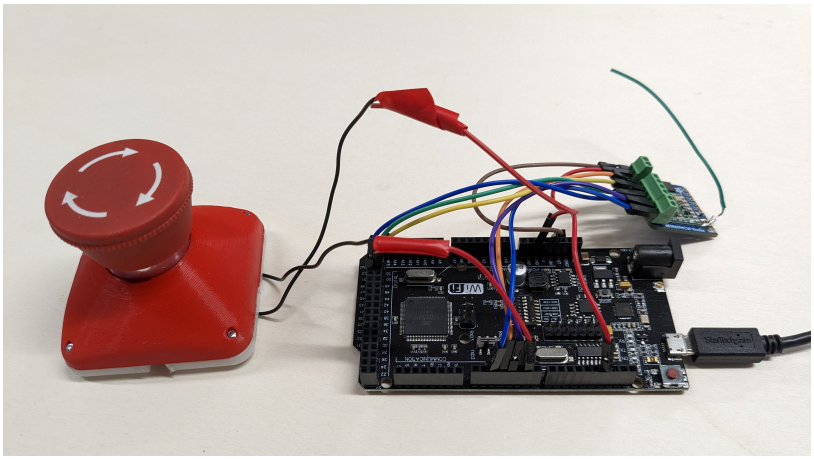

Figure 3.2: USB Radio Transceiver Dongle.

The Gimbalscope is shown in Figure 3.1. It features a scissored-pair DCMG atop the handle. Each flywheel is mounted to a gimbal motor, which itself is mounted to a structure attached to the central gimbal servo. Batteries are stored in the central column, which also serves as the device's handle. A momentary switch and push button are input methods, placed at the user's index finger and thumb positions. The thumb push button controls a front-facing laser pointer. The bottom section houses the majority of electronics required to operate the device. The Gimbalscope makes use of multiple Arduino microcontrollers and peripherals. The Gimbalscope is remotely operated from a PC using a digital radio communication protocol. This is facilitated with the USB transceiver dongle seen in Figure 3.2. the Gimbalscope's upper gimbals and flywheel motors operate at a nominal 12V, while the electronics and central gimbal servo operate at 5V. A complete circuit diagram is given in Figure 3.3.

3.1 Onboard Arduinos

The Gimbalscope uses an onboard Arduino Mega 2560 and an Arduino Micro as programmable microcontrollers, connected via the serial UART pins. The Arduino Micro is a dedicated radio operator. The Arduino Mega is the primary microcontroller, governing gimbal rotation, flywheel speed, user input, and orientation tracking. I programmed the Arduinos using C and uploaded the code to the boards using the Arduino IDE.

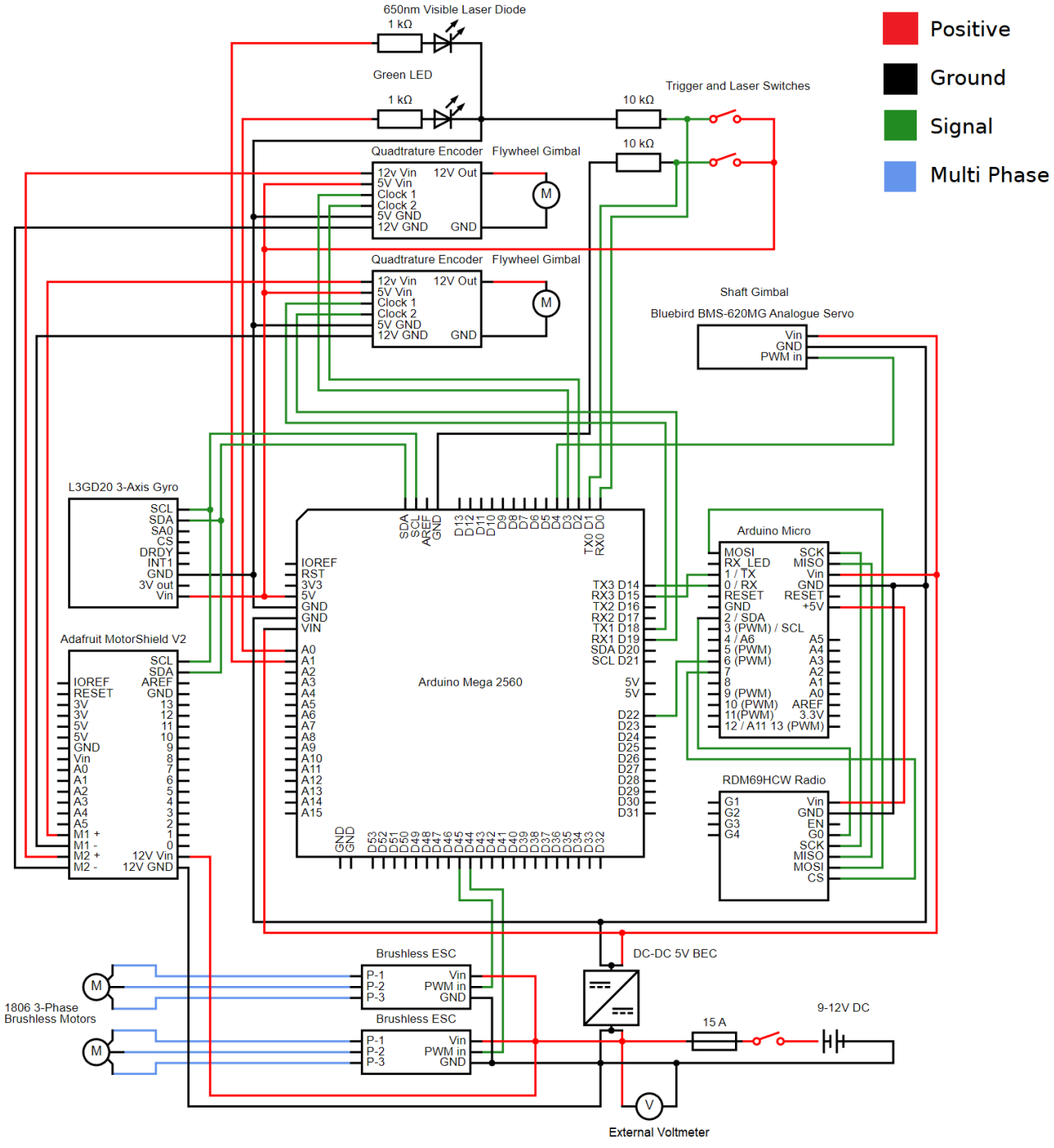

Figure 3.3: Gimbalscope Onboard Circuit Diagram ⟨req 8⟩

Arduino Mega 2560

An Arduino Mega 2560 runs the primary control loop of the Gimbalscope. It controls all other onboard components except for the RDM69HCW radio transceiver. I chose the Arduino Mega as the primary microcontroller for this project because of its number of interrupt pins, serial ports, and compatibility with standard shields. The control loop runs at a 'best effort' rate to control attached components as precisely as possible. The Arduino Mega features six interrupt pins, two of which are used for the SDA and SCL I2C pins. This is sufficient for the four pins required to receive interrupts from the upper gimbal motors' quadrature encoders. This would not be possible with other common boards such as the UNO and Leonardo. Software serial was not appropriate due to the performance requirements of this real-time control system. The open-source design and ubiquity of Arduino boards guarantee their accessibility ⟨req 7⟩.

Arduino Micro

An Arduino Micro serves as a dedicated controller for the onboard RDM69HCW radio transceiver. I found that the Micro's small form factor and low weight make it ideal for this purpose. There are two reasons for the existence of this controller. Firstly, the radio requires an interrupt pin, and the Arduino Mega does not have sufficient pins while operating the two quadrature encoders and I2C bus. Secondly, the Micro frees up processing time for the Arduino Mega. Sending and receiving radio commands is a relatively time-expensive process. By delegating this task, the control loop is able to run at a greater frequency, granting improved gimbal control.

Motorshield

An Adafruit Motorshield V2 is mounted to the Arduino Mega via its SDA and SCL pins, utilising the I2C communication bus. The Motorshield is capable of taking an input voltage of between 6V and 12V. The Motorshield is used as a motor controller to actuate the upper gimbals, composed of two 12V brushed micro metal gear motors with a 100:1 reduction ratio.

I trialled two alternative motor controllers during development. These were the SparkFun Dual TB6612FNG Motor Driver (3.2A peak) and the BBB Beetleweight Brushed ESC v3 (13.0A peak). Both controllers could handle 12V, but issues arose which made them unsuitable gimbal motor drivers.

Despite its advertised peak current, the SparkFun driver did not perform well when commanded to suddenly stop or reverse an attached motor's direction. The back-EMF frequently overloaded its H-bridge MOSFET, releasing smoke in the process. Not only did this make for an unreliable gimbal driver, but it was dangerous to users.

To attempt to rectify this issue, I tested the heavier-duty BBB ESC. Designed for use in combat robotics, this ESC had no such reliability issues. Despite this, the ESC's firmware did not allow for sudden changes in motor direction, most likely for safety reasons in its intended use case. Changing motor direction required sweeping the input PWM duty cycle from 45% to 55% at a minimum rate of 1% per 2ms. This was not conducive to fine motor control. Furthermore, this ESC is not of standardised design nor readily available outside the United Kingdom. As such, if I were to use it, it would hinder the project's goal of using accessible components.

The Motorshield struck a balance between these other controllers. Instead of using an Arduino's PWM pins, the shield has a dedicated PWM driver chip, handling all motor speed controls over I2C. Despite its H-bridges being rated for 3A peak current, the shield's internal kickback protection diodes proved to be reliable, allowing for high-resolution motor control and sudden halts. The Motorshield supports centre braking, and its open-source design guarantees its accessibility ⟨req 7⟩, ⟨req 9⟩.

3.1.1 Power

The Gimbalscope uses a pair of Tattu 3s 450mAh LiPo batteries in parallel as its onboard power supply (total 900mAh capacity) ⟨req 2⟩. A battery is shown in Figure 3.4. The LiPos deliver a nominal 12V and power the upper gimbal motors via the Motorshield and the flywheel motors through a pair of brushless ESCs. Per their specifications, the microcontrollers and central gimbal servo run at 5V. This is supplied using a BEC (Battery Elimination Circuit); a DC-DC voltage regulation component.

Section 2.2.5 describes the safety issues of LiPo batteries. To insulate against lithium fires, I packed the batteries in multiple layers of fire-retardant woven fibreglass, shown in 3.5. This had the added benefit of protecting the batteries against puncturing inside the Gimbalscope. Furthermore, I fitted a *'removable link'* with inbuilt fuse to the Gimbalscope, made using a section of 15A car fuse and xt-30 connector,

Figure 3.4: Tattu 3s 450 mAh LiPo with xt-30 connector.

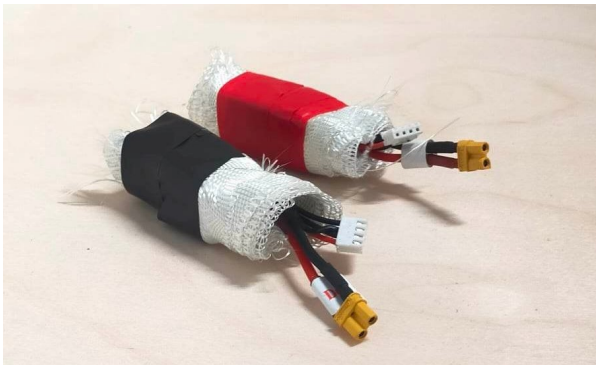

Figure 3.5: Pair of Tattu 3s 450 mAh LiPos packed in woven fibreglass.

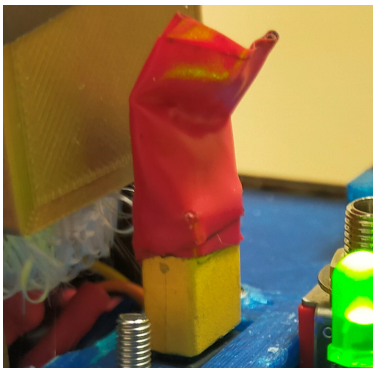

Figure 3.6: Removable xt-30 15A fuse link.

shown in Figure 3.6. Plugging the link into the device completes its power circuit. The fuse provides over-current protection and safeguards against short circuits. LiPos can become unstable if discharged too low. To prevent this, I wired a mini digital voltmeter with an LED display across the terminals of the power supply and mounted to it the rear of the Gimbalscope. This let me know when the batteries should be replaced ⟨req 9⟩.

3.2 Flywheel Design and Operation

Each flywheel is 3D printed and composed of uniformly solid PLA, with a diameter of 50mm, height of 15mm, weight of 30g, and a concave press-fit inset to house a brushless motor in the centre (Figure 3.7). Each 1806 2300KV brushless motor weighs 18g and is controlled by an open-standard 30A BLHeli-S 2-4S Oneshot ESC. Assuming the density of the brushless motor's rotor is similar to PLA, each flywheel has a moment of inertia of 9.4 x 10 $^{-6}$ $kg\,m^2$ in its axis of spin, and has approximate maximum speed and angular momentum of 27,000 RPM and 1.6 $kg\,m^2s^{-1}$ respectively.

As a result, given that the gimbal motors have an angular velocity of 400° s^{-1} and move through 180°, the Gimbalscope is able to produce a parabolic torque with an approximate peak of 22.3Nm over the course of 450ms. Without the PLA flywheels, under the same conditions, the Gimbalscope would produce an approximate peak torque of 0.150Nm. This maximum torque is greater than what is possible with the GyroCube, iTorqU, and J M Walker's device [17][18][34].

It should be noted that a greater torque magnitude is needed due to the Gimbalscope's mass. The Gimbalscope is larger and weighs more than Walker's device, at 912g to 198g [34]. I calculated the approximate moments of inertia about the x, y, and z axes to be 1.8 x 10^{-2}, 1.9 x 10^{-2}, and 1.8 x 10^{-2} $kg\,m^2$ respectively, using a process described in section 3.4. This is an order of magnitude greater than the moments of inertia of J M Walker's device at 1.2 x 10^{-3}, 6.5 x 10^{-3}, and 4.6 x 10^{-3} $kg\,m^2$ for the x, y, and z axes respectively. As such, larger torques are required to overcome the Gimbalscope's inertia. Note that inertial measurements will change when the gimbals are in motion. Furthermore, since the Gimbalscope is designed to be held with a full-hand grip instead of with a pinch, haptic cue torque must be large enough to influence a user's kinetic chain up to the wrist.

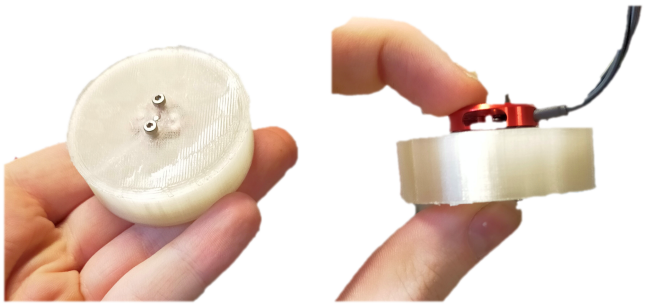

Figure 3.7: PLA flywheel with a press-fit brushless motor.

The flywheels went through multiple design iterations before their final form. J M Walker's devices did not use flywheels, instead relying on the inertia of the rotors of the brushless motors [33] [34]. However, these devices were comparatively light relative to the Gimbalscope due to their lack of onboard components. If the Gimbalscope did not use its printed flywheels, due to the inertia of the device, the angular impulse imparted on its body would be insufficient to be perceived by all users. Figure 3.8 shows a sample of flywheel designs trialled during development. It should be noted that the present gimbal motor mount was a limiting factor for flywheel designs during development. As such, I designed mounts and flywheels in parallel. All mounts are 3D printed.

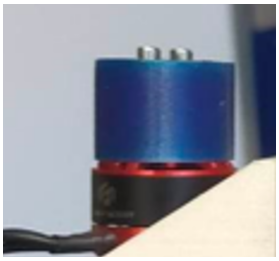

(a) Test mass designed to initially investigate motor behaviour.

(b) M12 metric nut mounted to threaded Ninjaflex filament flywheel.

(c) M14 metric nut mounted to threaded flywheel attached with motor manufacturer's prop shaft and bolt.

(d) M28 metric nut mounted to threaded flywheel press-fit over the brushless motor.

Figure 3.8: Sample of flywheels trialled during the Gimbalscope's development.

To accommodate the increasing size of flywheels, I designed several iterations of the flywheel gimbal motor mounts. The iterations can be seen in Figure 3.9. The final flywheel design is stable across the full range of motor saturation and, as such, can safely produce the greatest range of torques.

Subfigure 3.8a was the first mass designed to sit atop one of the brushless flywheel motors. I created it with the purpose of understanding how the vibration and acoustic characteristics of the motor change with an object mounted to it. The mass was not designed to be press fit, instead featuring a concave section and holes to secure it to the top of the motor with M2 metric bolts. Despite the test mass increasing the perceptible torque of the Gimbalscope, spinning the motor at even 20% saturation would cause loud noise and vibrations throughout the system. This was not desirable.

Two factors were subsequently investigated to attempt to reduce vibration, material hardness and motor speed; on the basis that a less rigid material would produce a dampening effect. A greater and more radially distributed mass would grant the flywheel a more advantageous moment of inertia for

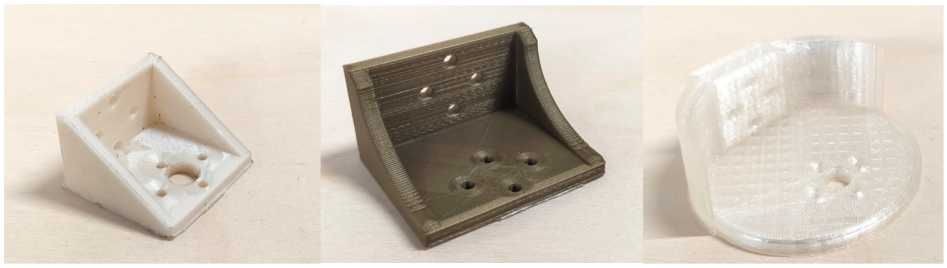

Figure 3.9: Gimbal flywheel mount design iterations.

generating torque. The result is Subfigure 3.8b, a 3D printed Ninjaflex TPU threaded mount with an attached M12 steel metric nut. This flywheel performed better than the previous design as it produced greater output torque. However, the Ninjaflex material had a negligible vibration-dampening effect and, even at lower speeds, the device was still uncomfortable to use. A third iteration, (depicted in Subfigure 3.8c) was tested with similar motivations. This mass was mounted to the motor using the prop adapter machined by the manufacturer, with the goal of eliminating an imperfect mount as a causal factor for vibration. However, there were no noticeable performance improvements.

I created a device named the mechanical analysis module to characterise the Gimbalscope's vibrations (described in Section 3.19). With the aid of this module, I discovered that vibrations were more prevalent when the centre of mass of the flywheel was greater than the height of the motor. As such, the current flywheel and that depicted in Figure 3.8d were created to keep the setup's centre of mass as low as possible.

The fourth flywheel in Subfigure 3.8d weighed 120g and could create substantial torque at just 10% saturation. However, at speeds greater than this, the device became uncontrollable and unsafe to use. Furthermore, because of the flywheel's mass, the gimbal motors did not have enough torque to remain stationary during centre-braking and required the PID system (discussed in 3.3) to continuously adjust motor power, overheating the gimbal motors. Due to its lower mass and greater width, the final flywheel design has a more optimal moment of inertia than this flywheel. The gimbal motors are stable in their operation and at rest. The current flywheel's balanced and press-fit design results in lower systemic vibrations, lower noise, and greater safety ⟨req 9⟩.

3.3 Gimbal Design and Operation

The Gimbalscope features a pair of standard 12V micro metal geared motors with quadrature encoders at 100:1 reduction ratio to actuate the flywheel gimbals. A Bluebird BMS-620MG Metal Gear Analogue Servo is used to actuate the central gimbal. This arrangement is highlighted in Figure 3.10 ⟨req 7⟩.

As stated in section 3.1, each quadrature encoder is connected to a pair of interrupt pins on the Arduino Mega. Hall-effect sensors provide 12 counts per revolution of the motor shaft. Each count triggers an ISR (interrupt service routine), which increments or decrements a volatile counter depending on the direction of rotation. Every update loop, this counter is used to calculate the current orientation of the gimbal motors. A PI (proportional integral) controller sets the gimbals' target orientation and angular velocity. Contrastingly, the orientation of the central gimbal servo is specified using a PWM signal from a digital pin on the Arduino Mega. Unlike the flywheel gimbals, it has no closed-loop control.

The PI system defines gimbal motor angular velocity as RPM. To estimate a gimbal's RPM, a rolling average of the last 100 polls is calculated every cycle of the main update loop. This informs the Adafruit Motorshield, adjusting supplied motor power by a specified gain factor.

During development, I encountered several issues with gimbal control methods. The Gimbalscope's DCMG is arranged in a scissored-pair setup. This requires the flywheel gimbals, at any one time, to be of opposing orientation and equal and opposite angular velocity. If this is not the case, the generated torque may not be isolated to a single axis as demonstrated in Figure 2.8b.

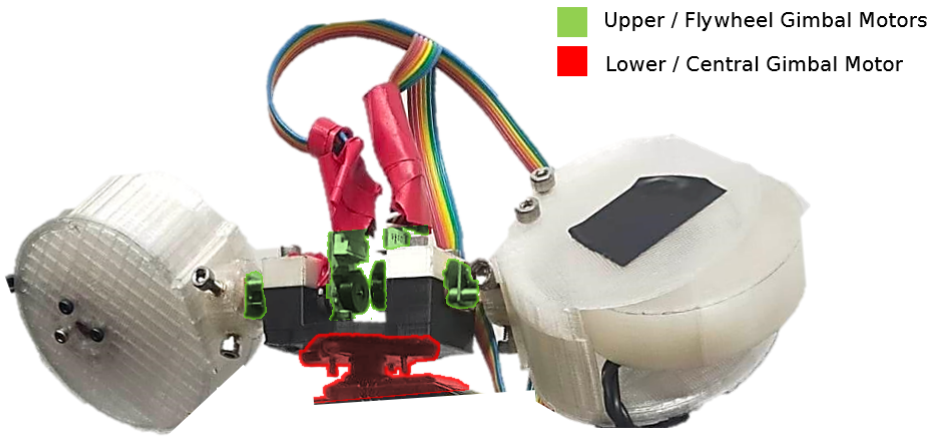

Figure 3.10: Highlighted Gimbal Motors

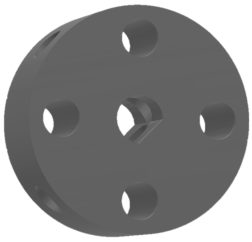

(a) D-Shaft coupler CAD model

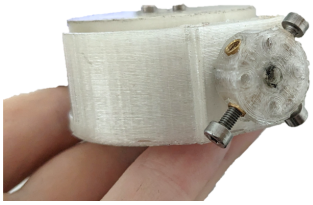

(b) D-Shaft coupler after prolonged use.

Figure 3.11: Upper Gimbal D-Shaft Coupler

Gimbal synchronisation problems occur when the Arduino Mega cannot service encoder interrupts on demand, resulting in ambiguous torques. To rectify this, I wrote the ISRs to be as efficient as possible, avoiding any reference to complex datatypes. Additionally, I used the PI controller to limit gimbal motor RPM to that of an experimentally-determined reliable maximum speed - one in which the tracked orientation during actuation does not drift or falter over time. Furthermore, I designed the system such that serial read/write operations between the Arduino Mega and Arduino Micro radio operator are not performed while the gimbals are in motion. This is because the serial UART uses interrupts, which take priority over encoder ISRs. Instead, I implemented a spooler to manage radio commands between the Arduino Micro and Arduino Mega ⟨req 4⟩.

Mechanical factors also caused synchronisation issues. As described in Section 3.7, the flywheels are connected to the gimbal motors using 3D-printed PLA shaft couplers. Slipping on these shaft couplers causes the orientation of the flywheels to differ from that of the motor shaft. As such, I designed shaft couplers to press fit the 3mm diameter D-shaft of an n20 gear motor and feature threaded metric M3 heat inserts to secure the connection with grub screws. The shaft coupler is shown in Figure 3.11 ⟨req 4⟩. However, over prolonged use, the PLA D-shaft socket did not retain its original shape due to deformation, requiring frequent replacements, evident in Subfigure 3.11b).

The central gimbal servo is connected to a 5V BEC. It receives a PWM signal from one of the Arduino Mega's digital pins, as seen in the circuit diagram Figure 3.3. Due to the lack of closed-loop control and low resolution offered by the BMS 620MG, I found it to be unsuitable for precise movements, unlike the flywheel gimbals. I chose to use a servo as the central gimbal actuator due to having no free interrupt pins to support a third closed-loop motor and encoder when the Adafruit Motorshield is used. An early prototype of the Gimbalscope utilised a central motor and encoder as shown in Figure 3.12. It should be noted that this version did not use the Motorshield and was instead using BBB Brushed ESCs connected to digital PWM pins.

I made the decision to not use the Motorshield's dedicated 5V servo pins. This is because power is supplied via the Arduino's onboard voltage regulator, and the current drawn by the servo exceeds the safety rating. I found the gimbal servo to 'twitch' while powered, causing unintended haptic sensations. This was due to a damaged potentiometer. The twitch was mitigated by only sending a signal to the

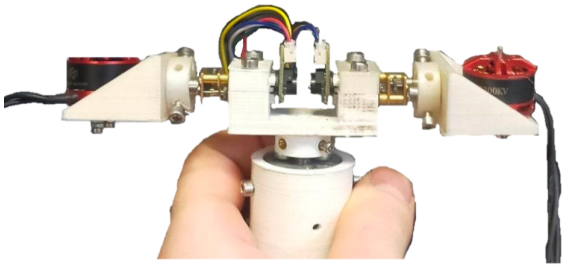

Figure 3.12: Early Gimbalscope Prototype with motor and encoder pair for central gimbal control.

servo when it had to be to be rotated, centred, or braced (powered but stationary) ⟨req 5⟩. Bracing is needed as large horizontal torques can overcome the resistance of the servo gearbox.

The process of generating a torque is composed of three states; **Load**, **Fire**, and **Reload**. Progression to the next state is locked until both flywheel gimbals have completed their movements. The **Load** state instructs the flywheel gimbals to move to their defined start orientations at a slow speed (i.e θ and $-\theta$ for a lateral torque orthogonal to the device's vertical axis) and sets the central gimbal's orientation for all three states. The **Fire** state instructs the flywheel gimbals to rotate to a pair of target orientations (i.e $-\theta$ and θ) at a given angular velocity, generating a perceptible torque. The **Reload** state instructs the flywheel gimbals to slowly move back to their start orientations.

3.4 Calculating Moments of Inertia

Calculating the moments of inertia of certain objects is relatively simple given some assumptions. For instance, the radial inertia I_{zz} of a uniformly dense flywheel with mass m_F and radius r may be given by:

$$I_{zz} = \frac{1}{2} m_F \, r^2 \tag{1}$$

However, it is much more complicated to calculate the inertia of irregular 3D volumes with uneven weight distribution. Solutions exist within CAD packages [3] [4], but the software is often proprietary and requires a specially designed model. As such, I wrote a script in Python to numerically estimate the x, y, and z moments of inertia of an object.

An object may be treated as a 3D arrangement of point masses. The moments of inertia in the roll, pitch, and yaw axes may be calculated by summing over every point relative to the object's centre of mass, as described below:

$$I_{xx} = \sum_k m_k (y_k^2 + z_k^2) \tag{2}$$

$$I_{yy} = \sum_k m_k (x_k^2 + z_k^2) \tag{3}$$

$$I_{zz} = \sum_k m_k (x_k^2 + y_k^2) \tag{4}$$

To perform these calculations in Python, I first had to create a volume of point masses. I accomplished this by using the Drububu Online Voxelizer to convert an OBJ model of the Gimbalscope to a list of voxel coordinates [1]. Knowing the height of the Gimbalscope, I perform a scale factor operation on the voxel coordinates, converting the points to SI units. The ∼15K point masses are displayed in Figure 3.13.

Once imported, to improve the accuracy of the approximation, I marked the bottom, middle, and top sections to have masses of 412g, 150g, and 350g respectively - values close to the actual mass of each section. I defined point masses in each section to have mass m_p, given by the equation:

$$m_p = \frac{m_s}{N} \tag{5}$$

where m_s is the mass of the section and N is the number of points in a section. These volumes are coloured and shown in Figure 3.14.

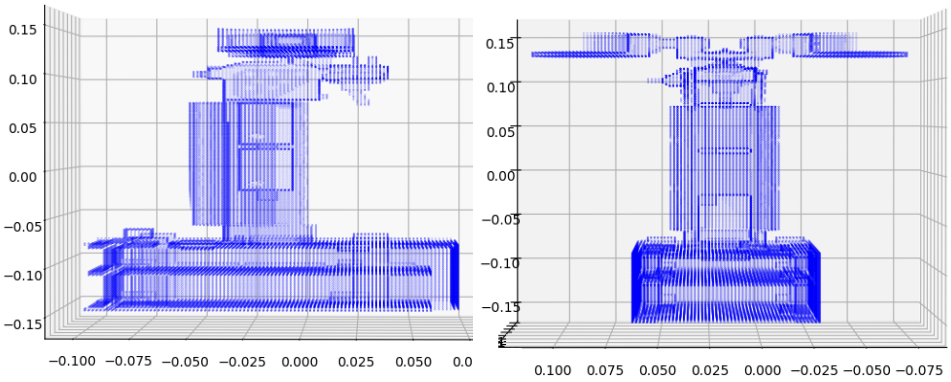

(a) Side View (b) Front View

Figure 3.13: Gimbalscope point masses displayed in matplotlib 3D scatter plot.

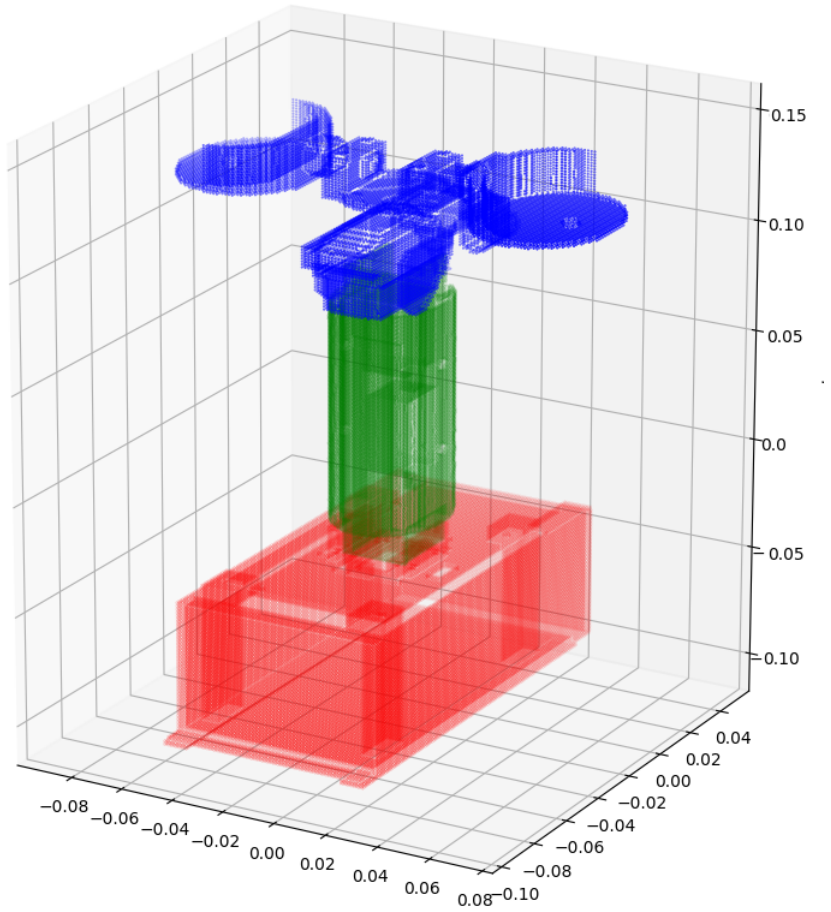

Figure 3.14: Gimbalscope point masses displayed in matplotlib 3d scatter plot, colour coded by part.

I calculated the approximate moments of inertia about the x, y, and z axes to be 1.8 x 10^{-2}, 1.9 x 10^{-2}, and 1.8 x 10^{-2} $kg\,m^2$ respectively.

3.5 Wireless Communication

The Gimbalscope sends and receives information via 900MHz radio facilitated by a pair of Adafruit RFM69HCW transceiver modules ⟨req 2⟩. The USB radio dongle (Figure 3.2) has a circuit diagram shown in Figure 3.15. Commands and telemetry are transmitted to and from the Gimbalscope. Wireless communication is handled using a request / acknowledge paradigm. The dongle receives commands from a Unity environment running on the controller PC with the aid of the Ardity package, written in C#.

Arduino parses characters in the 8-bit ASCII format, whereas C# and .NET parse characters in the 16-bit UTF-16 format. To avoid miscommunication, commands are described as a string with each character explicitly cast to 8-bit representation. Each command is composed of a fixed length of bytes specifying the command function and a variable length of trailing bytes specifying parameters. The resultant stream of bits is transmitted via radio utilising Manchester encoding. The command is received and decoded by the Arduino Micro's radio transceiver and spooled via UART to the Arduino Mega where it is parsed. This allows the Unity environment to communicate with the Arduino. This process is reversed to send telemetry, requests, and acknowledgements back to the controller. It is necessary to allow a delay of ∼2ms between read operations to give time for the serial buffer to populate.

The Gimbalscope features a wireless emergency stop, activated by the red safety button in Figure 3.2 and represented by the switch in Figure 3.15 ⟨req 9⟩. Pressing this button sends a command to the Arduino Micro, setting a digital pin connecting to the Arduino Mega to high. This pin is polled by the Arduino Mega every update loop. If it detects a high input, a flag is raised to halt all gimbal motors and activate the flywheel brakes. Regular operation is resumed by resetting the switch button. The emergency stop procedure is handled this way to avoid waiting for the command to be spooled in a queue with non-emergency commands. The complete circuit diagram 3.3 shows the serial UART and emergency pin connections.

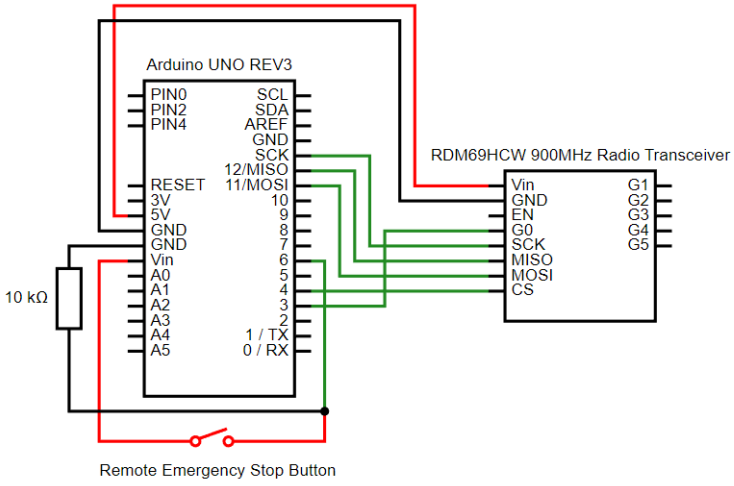

Figure 3.15: Radio Transceiver Dongle Circuit Diagram ⟨req 8⟩.

During development, I trialled utilising a wireless LAN using the ESP8266 WiFi breakout board and TP-Link TL-WR710N pocket router to facilitate wireless communication. I found this to be less reliable than digital radio. The router did not provide the plug-and-play capability offered by my radio dongle, nor did it provide the range.

3.5.1 Orientation Tracking

Gimbalscope spatial orientation tracking uses an Adafruit L3GD20 three-axis Gyro connected to the Arduino Mega via I2C. The three-axis gyro is located centrally in the Gimbalscope's electronics bay and measures instantaneous angular velocity. An orientation estimation is given by numerically integrating the measurement on each update loop of the Mega. Drift in the gyro's readings is mitigated through a calibration process in which the device is held stationary, and a sample of 1000 measurements is taken over a known time. The mean drift of angular velocity per second is calculated and used to augment future measurements.

I initially planned to use the MPU 6050 9-DOF IMU, however, the boards I trialled were electrostatically-sensitive and would often cease functioning inside the Gimbalscope. This caused orientation tracking to fail frequently and IMUs had to be regularly replaced. However, I found a use for the MPU 6050 in creating the Mechanical Analysis Module (section 3.9).

3.6 User Input

The Gimbalscope features a trigger and thumb button for user input, located at the index finger and right-hand thumb positions. A green LED is lit when its buttons may be pressed. The following inputs are available:

- **Cue Request**: A haptic cue may be requested by quickly pulling and releasing the trigger akin to a mouse click.
- **Target Selection**: In the target identification experiment, a target may be selected by holding the trigger for at least one second.
- **Laser Pointer**: The onboard class 1M laser pointer may be activated by holding the thumb button.
- **Gyro Calibration**: The onboard three-axis gyro may be re-calibrated by holding the trigger and thumb button for at least one second. This also activates the laser pointer.

The Gimbalscope uses a class 1M laser pointer because its point is safe for viewing with the naked eye ⟨req 9⟩. Despite this, the laser should not be magnified or aimed at other people.

3.7 Chassis Fabrication

The Gimbalscope is designed to resemble an object familiar to most users to afford its intuitive use. As such, I designed it to mimic the shape and balance of a power drill and provide feedback similar to that of a joystick ⟨req 10⟩. I designed the Gimbalscope to be light enough to be comfortably handheld and for easy maintenance ⟨req 1⟩. Figure 3.16 shows the design influences.

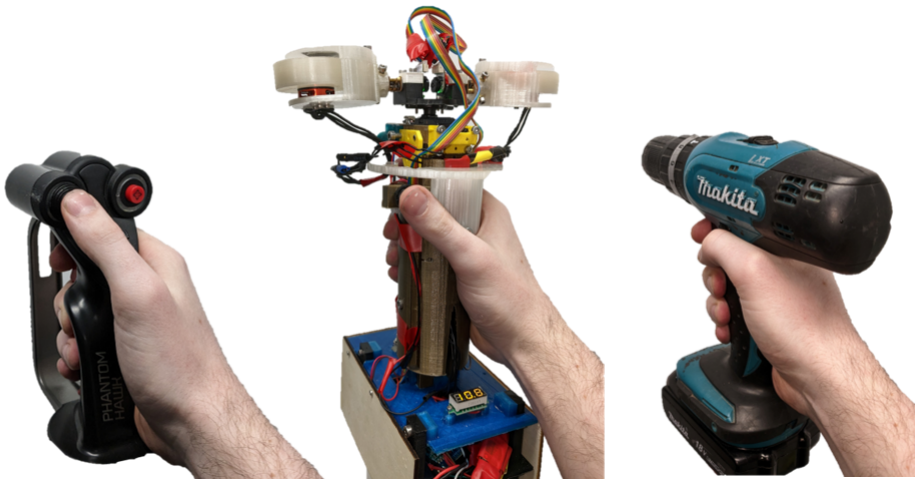

Figure 3.16: Gimbalscope form factor influences. Joystick (left), Gimbalscope (centre), and a power drill (right).

I designed the Gimbalscope as per the Canadian hand tool ergonomics guidelines [10]. It weighs less than a typical hand drill at 912g and is balanced along its vertical axis, requiring minimal effort in the wrist and forearm to hold in a usable position. The straight handle allows for safe applications of force perpendicular to the wrist ⟨req 9⟩.

All structural components of the Gimbalscope are 3D printed and feature self-tapping metric machine screw holes for M2, M3, and M4 bolts. The device can be non-destructively disassembled and re-assembled. I found this to be a significant benefit during development, as new components could be

fabricated and installed with relative ease. All components are designed to be printed without requiring supports. An assembled CAD can be seen in Figure 3.17, where protruding cylinders indicate screw holes to be subtracted.

I designed components using Microsoft 3D Builder and Autodesk Fusion 360. 3D Builder is a low-fidelity CAD package that allowed me to rapidly prototype components. Successful parts were remodelled and collated in Fusion 360, which enforces consistent design standards. This helped ensure that printed components could be tightly slotted together during assembly, increasing structural integrity. Despite the fact that Fusion 360 is a proprietary piece of software, educational licenses are available and the vast majority of design was carried out with 3D Builder. Note that .stl files can be exported with the free version of Fusion 360.

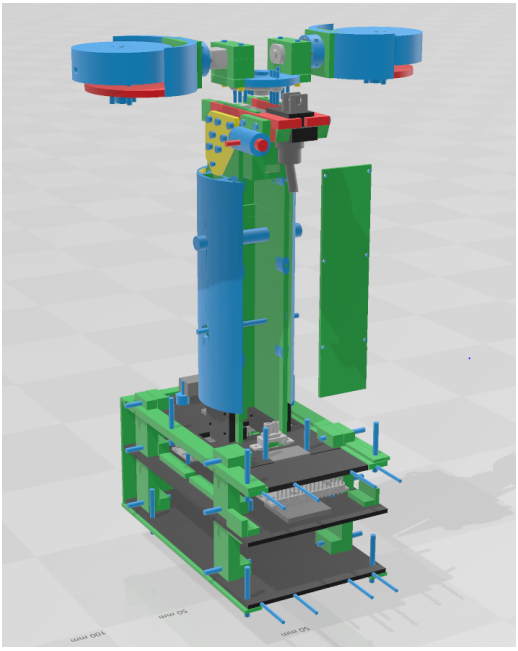

Figure 3.17: CAD of the final iteration of the Gimbalscope, shown in 3D builder. Protruding cylinders indicate machine screw holes.

3.8 Command and Control Environment

Command and control of the Gimbalscope is dictated through a Unity environment running on a computer with an attached radio dongle. The environment provides a GUI for users to set parameters and send commands, such as setting gimbal angular velocity or ordering the device to enter its **Fire** state. The GUI is shown in Figure 3.18. Commands may be sent to the Gimbalscope through the environment's GUI or requested by the device's user ⟨req 3⟩.

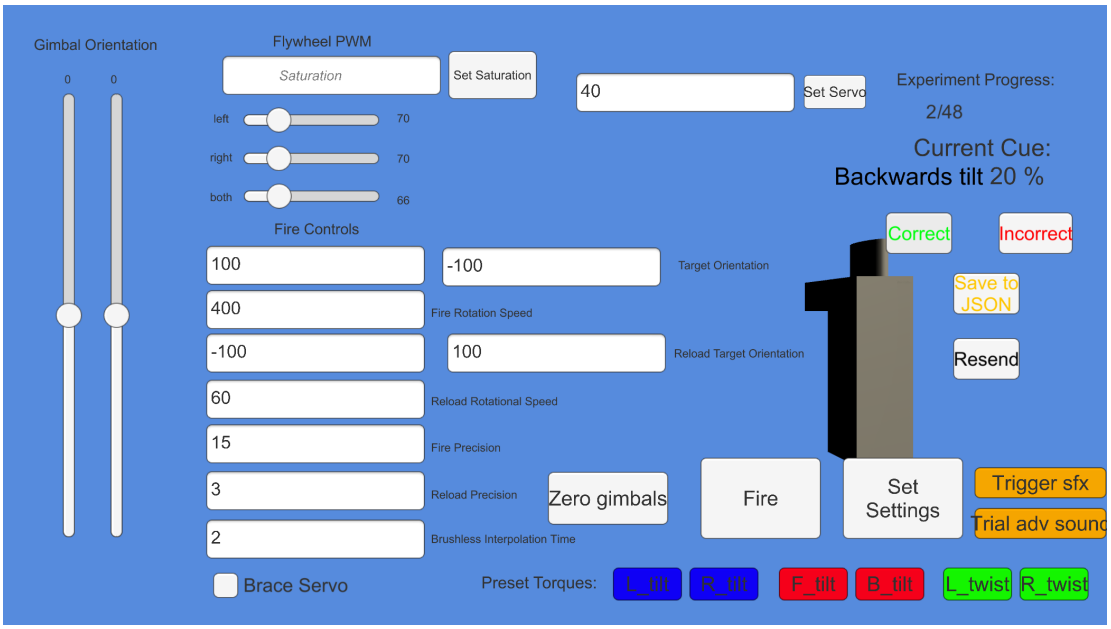

Figure 3.18: Unity command and control environment during the threshold of discrimination experiment.

I used Unity because of its 3D environment and comprehensive API, granting a pre-existing context in which to perform orientation resolution calculations with respect to target position vectors. This was crucial for facilitating the target identification experiment described in section 4.3. In the environment, the present orientation of the Gimbalscope tracked by its three-axis gyro is displayed with a graphical 3D representation. This allowed me to check for discrepancies between the estimated and actual orientation of the device in real-time, and re-calibrate the three-axis gyro if needed.

Orientation telemetry is received as Euler angles. However, Euler angles are susceptible to gimbal lock - a situation in which axes of two angular rotation components are aligned, resulting in no unique solutions to a given orientation. Unity provides a robust utility to convert Euler angles to quaternions. Quaternion rotations can be composed and interpolated without the risk of encountering gimbal lock, making them a more robust and reliable method for representing orientation in 3D space. As such, orientation resolution calculations are performed using quaternions. Using the radio transceiver, the Gimbalscope's Arduino Mega can offload orientation resolution calculations to the Unity environment, freeing up resources and keeping its control loop as fast as possible.

The existence of the command and control environment makes the Gimbalscope task-agnostic. It is not necessary to upload new code to the onboard Arduinos to perform a new task or experiment. The Gimbalscope is a general-purpose input/output device. As such, user experiments can be written entirely within the Unity environment, significantly reducing the time taken to design experiments and improving technical consistency across experiments.

Using Unity reduced development time compared to using a less comprehensive environment such as Processing. Furthermore, the accessibility of the Unity platform makes it easier for people who seek to reproduce the Gimbalscope to download, run, and make changes to the control software ⟨req 6⟩.

3.9 Mechanical Analysis Module

I designed the Mechanical Analysis Module to quantify the torque and vibration characteristics of the Gimbalscope. It is a component external to the Gimbalscope, consisting of an Arduino UNO and MPU 6050 IMU. The module connects to a computer via USB through a COM port. Telemetry is sent via the COM port at a baud rate of 28,800 and logged to a file by a Python script. Logged telemetry is analysed and plotted using the matplotlib Python package. Figures 3.19 and 3.20 show the module and its circuit diagram.

I designed the Mechanical Analysis Module as a low-cost and accessible alternative to the profiling equipment used to evaluate J M Walker's DCMG device [34] and the iTorqU 2.0 [17], described in section 2.1.4 ⟨req 6⟩ ⟨req 7⟩. The module aims to approximate the behaviour of a multi-axis force/torque sensor as well as a vibrometer.

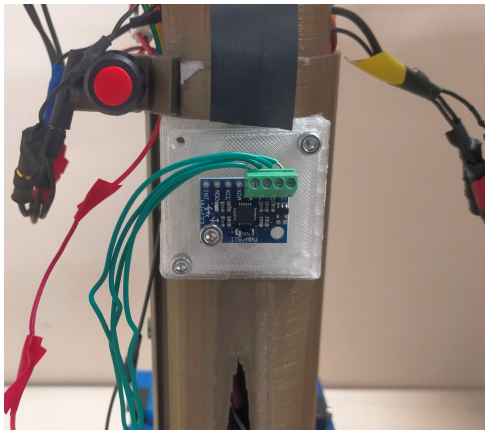

Figure 3.19: Mechanical Analysis Module

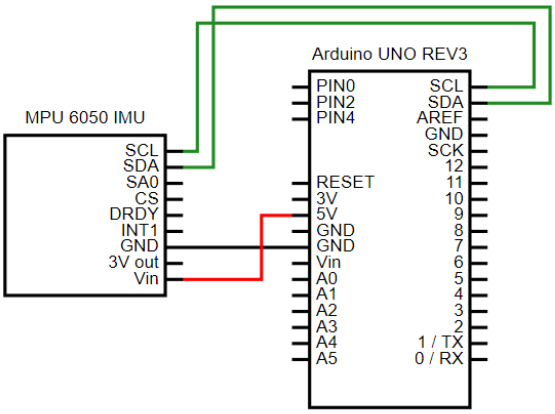

Figure 3.20: Mechanical Analysis Module Circuit Diagram

The MPU 6050 is a 6-DOF device featuring an accelerometer and MEMS gyroscope. As part of the analysis module, the accelerometer is used to record vibration telemetry, and the gyroscope is used to measure angular velocity as an analogue to torque. To ensure accurate telemetry, the module is bolted to the Gimbalscope's handle using a concave 3D printed mount, ensuring it is secure during operation. The mount ensures placement of the module on the Gimbalscope is consistent between trials.

The reliability issues I encountered with my MPU 6050 boards were inconsequential when used inside the Gimbalscope for orientation tracking. Since the module is external, if a board malfunctioned, I could quickly and easily replace it.

I found the Mechanical Analysis module to have two significant limitations. Firstly, the module can only measure the effect of a torque pulse on the Gimbalscope's orientation, not the moment itself. A reading can only be ascertained when the Gimbalscope is gripped lightly. As such, approximate torque must be mathematically calculated with the equations given in section 2.2.1. Secondly, paired with the Arduino Uno, I found that the module has a maximum accelerometer sample rate of 300 Hz. This limits the fidelity of readings when profiling high-frequency vibrations. However, this rate does not apply to the MPU's three-axis gyro, which could be sampled at 1KHz. These sample rates are below the advertised specification (1KHz and 8KHz for the accelerometer and gyroscope respectively). However, it is possible that the serial connection used to log data is a limiting factor.

Chapter 4

Experiment Design

Experiments designed to evaluate the Gimbalscope in a human context aim to investigate the following objectives:

1. Experiments **aim** to determine if the direction of the device's torques is perceptible to participants.

2. Experiments **aim** to reproduce the results of J M Walker's haptic DCMG perception study [34].

3. Experiments **aim** to determine the discrimination threshold for correctly perceiving directional torques.

4. Experiments **aim** to explore how participants use the device to identify and aim at a set of targets.

The above points are referenced when an experiment addresses an aim throughout this chapter, indicated using angle brackets: e.g. ⟨aim 1⟩.

I designed three experiments to quantitatively assess the Gimbalscope's performance in the hands of a human. The three experiments were performed sequentially, informing the design of the following study after evaluating the results of the previous. Each experiment was designed and ran using the Unity command and control environment. In all experiments, participants were asked to wear a full-face welding mask, both as a safety and control measure, ensuring that participants could not deduce the direction of the Gimbalscope by looking at the orientation of its gimbals. Participants could pause the experiment and remove the mask at any time.

Independent, dependent, and control variables are listed in each experiment's section.

4.1 User Study I: Torque Perception Test

The torque perception test was the first experiment I ran. Its primary aim was to investigate if the direction of the torque produced by the Gimbalscope is perceptible to participants when the device is held ⟨aim 1⟩. The secondary objective of the experiment is to attempt to reproduce the results of J M Walker's DCMG direction identification experiment [34] using the Gimbalscope ⟨aim 2⟩. Non-quantitatively, the study also aims to explore the language used by participants to describe the motions of the Gimbalscope.

4.1.1 Method

8 participants were tasked with identifying the direction of a range of torques induced by the Gimbalscope with varying directions and magnitude. Torque magnitude is a function of flywheel RPM. Isolated torques were induced clockwise and counter-clockwise about the pitch, yaw, and roll axes. Participants were asked to describe one of six possible directions in each trial.

Each participant was subject to 36 trials, with 2 trials for each of the 6 directions, for flywheel saturations of 20%, 30%, and 40% (generating 4.46 Nmm, 6.69 Nmm, and 8.92 Nmm of torque respectively). The order of trials was shuffled such that no identical haptic cues would be adjacent in sequence. A total of 288 trials were performed.

Figure 4.1: Torque perception test participant setup.

Participants performed the experiment seated and were asked to hold the Gimbalscope with their dominant hand. Participants rested their elbow on their knee or a stool depending on the most comfortable position (see Figure 4.1). Haptic cues are requested by pulling the momentary switch trigger on the device. Participants could request any number of haptic cues.

Before trials commenced, all 6 unique haptic cues were given at 30% flywheel saturation to familiarise participants with the Gimbalscope's torque pulses. Participants could request as many haptic cues as required to identify the torque direction.

Results of the torque perception test are presented and discussed in section 5.2.1.

Control Variables:

- Participants must wear the full-face welding mask to mitigate visual clues from gimbal orientation.
- Flywheel gimbal motor fire angular velocity is maintained at 400° s^{-1} to keep torque magnitude and duration consistent between trials.
- Central gimbal servo orientation is fixed during the fire sequence to prevent changes in torque direction.
- Gimbals return to an upwards-facing orientation between trials to prevent participants from deducing changes in gimbal orientation.
- Onboard LiPo batteries are fully charged before each experiment to prevent changes in flywheel RPM due to voltage drop.

Independent Variables:

- Magnitude of torque induced by the Gimbalscope.
- Direction of torque induced by the Gimbalscope.

Dependent Variables:

- Success or failure of the participant to identify direction of haptic cue.

4.2 User Study II: Threshold of Discrimination Test

The results of the torque perception test demonstrate that participants have the ability to reliably distinguish the direction of haptic cues given by the Gimbalscope (see section 5.2.1). Following this success, the threshold of discrimination experiment was designed. The experiment aims to investigate the saturation at which humans can no longer reliably identify the direction of a haptic cue ⟨aim 3⟩. The experiment's design is similar to the torque perception test, but over a larger set of trials conducted with smaller torque magnitudes. The experiment records the number of haptic cues requested by the participant as a measure of uncertainty.

Maximum flywheel saturation in this experiment was informed by the results of the torque perception test and the vibration profile sampled by the mechanical analysis module, described in section 5.2.1 and 5.1.2.

Based on participant feedback from the previous experiment, the threshold of discrimination test features unique audio cues to indicate when the Gimbalscope is prepared to deliver a haptic cue, as well as when the experiment is progressing to the subsequent trial. This is facilitated by the Gimbalscope sending a request to the Unity environment to play a sound through the PC's speakers. Furthermore, instead of describing the direction of torque, participants were asked to gesture the direction of the haptic cue with the Gimbalscope in hand. This is because participants used varying terminology to describe movements, requiring much clarification on behalf of the participant to ensure the correct result was recorded.

Results of the threshold of discrimination test are presented and discussed in section 5.2.2.

4.2.1 Method

13 participants were tasked with identifying the direction of a range of torques generated by the Gimbalscope, with torques generated in both directions about the pitch, yaw, and roll axes.

Each participant was subject to 48 trials, with 2 trials for each of the 6 directions, for flywheel saturations of 5%, 10%, 15%, and 20% (generating 1.12 Nm, 2.23 Nm, 3.35 Nm, and 4.46 Nm of torque respectively). The order of trials was shuffled such that no identical haptic cues would be adjacent in sequence. A total of 624 trials were performed. Participants were seated as in the previous experiment (see Figure 4.1). Using the trigger, participants could request as many haptic cues as necessary but were advised to request as few as possible before being certain of their answer. The number of cues requested in each trial was recorded. An audio cue indicated when a haptic cue became available to request.

Control Variables:

- Participants must wear the full-face welding mask to mitigate visual clues from gimbal orientation.
- Flywheel gimbal motor fire angular velocity is maintained at $400° \text{ s}^{-1}$ to keep torque magnitude and duration consistent between trials.
- Central gimbal servo orientation is fixed during the fire sequence to prevent changes in torque direction.
- Gimbals return to an upward-facing orientation between trials to prevent participants from deducing changes in gimbal orientation.
- Onboard LiPo batteries are fully charged before each experiment to prevent changes in flywheel RPM due to voltage drop.

Independent Variables:

- Magnitude of torque induced by the Gimbalscope.
- Direction of torque induced by the Gimbalscope.

Dependent Variables:

- Success or failure of the participant to identify direction of haptic cue.
- Number of haptic cues required for the participant to identify torque direction.

4.3 User Study III: Target Identification Test

The results of the previous threshold of discrimination test demonstrate the clarity and robustness of the Gimbalscope's torque pulses perceived by a human. In order to test the device in a use-case environment as a navigation aid, I designed the target identification test.

The target identification test aims to quantitatively explore if and how participants are able to use directional torque pulses to identify a target bearing in their frame of reference ⟨aim 4⟩. Participants are required to orient themselves towards this target bearing. Target bearings are represented in the real world with printed sheets of paper. The Unity command and control environment records the path the participant takes to identify a bearing. This is shown in Figure 4.2. Participants should feel a 'pull' torque directly towards the target bearing.

The results of the target identification test are plotted and visualised inside a 3D sphere. Results are displayed and discussed in section 5.2.3.

(a) Real World Gimbalscope Orientation. (b) Unity Environment Orientation Representation.

Figure 4.2: Participant performing target the identification experiment. Gimbalscope orientation is tracked and transmitted to the Unity command and control environment.

4.3.1 Method

6 participants were tasked with using the Gimbalscope as a navigation aid to orientate themselves towards a set of 7 target bearings, located at 045°, 090°, 135°, 180°, 215°, 270°, and 315° from the participant's start orientation. Each bearing was to be identified exactly once by each participant, with 7 trials per participant, totalling 42 trials across the whole experiment. The order of trials was randomised for each participant.

Target bearings are located on the horizontal plane. To help the participant understand the objective of the experiment, targets were printed and pinned to the walls of the testing room. Cues generate a torque pointing to the target bearing. Participants may request any number of haptic cues using the Gimbalscope's trigger. When a participant requests a haptic cue, a unique audio cue is played as the device enters its **Load** state, before playing a separate cue as the device subsequently enters its **Fire** state.

Cue torque is constant throughout the experiment, with 400° s^{-1} gimbal motor angular velocity and flywheel saturation fixed to 53% (11.81 Nm). I found 53% flywheel saturation to be a local minimum point in the Gimbalscope's vibration profile, determined using the mechanical analysis module and discussed in section 5.1.2. I chose this relatively high saturation because participants would be standing while holding the device, and as such, hold the device with a stiffer wrist. This can reduce the perception of torque.

The orientation of the Gimbalscope is streamed to the Unity control environment at a rate of 5Hz. Additionally, orientation keyframes are sent to the control environment upon each cue request. This data is logged.

Before each trial, the participant is required to calibrate the Gimbalscope's three-axis gyro. This is accomplished by activating the laser pointer and aiming the device at a target placed at bearing 000° while holding the trigger.

Throughout the experiment, participants wear the welding mask. This is because participants may deduce the target bearing by the orientation of the central gimbal. The mask also hides any discrepancies

that arise between the actual target's bearing and the Gimbalscope's estimated target's bearing due to gyro drift, potentially confusing the participant.

Control Variables:

- Participants must wear the full-face welding mask to mitigate visual clues from gimbal orientation.
- Flywheel gimbal motor fire angular velocity is maintained at $400° \ s^{-1}$ to keep torque magnitude and duration consistent between trials.
- Flywheel saturation is maintained at 53% throughout the experiment to maintain torque magnitude. Changing flywheel speed during trials could lead the participant to attempt to deduce proximity to the target bearing using sound and vibration.
- Central gimbal servo orientation is fixed during the fire sequence to prevent changes in torque direction.

Independent Variables:

- Choice of the target bearing.

Dependent Variables:

- Orientation path taken by the participant to orientate towards the target bearing.
- Time taken by the participant to orientate towards the target bearing.
- Number of haptic cues required by the participant to orientate towards the target bearing.
- Orientation of the Gimbalscope when a haptic cue is requested by the participant.

Chapter 5

Critical Evaluation

The critical evaluation chapter is split into three sections. Firstly, a mechanical evaluation is given, describing the behaviour of haptic cues and discussing the Gimbalscope's vibration profile. Secondly, a user evaluation is given, discussing the results of experiments described previously in Chapter 4. Thirdly, an evaluation of miscellaneous aspects of the device is presented at the end of the chapter.

5.1 Mechanical Evaluation

5.1.1 Angular Velocity Investigation

Since I did not have the equipment to directly measure the torque produced by the Gimbalscope, I instead used the mechanical analysis module to gather orientation data of the device during haptic cues. When the Gimbalscope is held freely about its centre of mass, its instantaneous angular velocity is proportional to the instantaneous torque of the haptic cue. The motivation for this investigation is to experimentally demonstrate that haptic cues can be isolated to a single torque axis, as described by the mathematical derivation in section 2.2.1.

To perform the investigation, I held the Gimbalscope lightly between my thumb and forefinger, allowing it to move relatively freely in my hand. The flywheels were spun to 20% saturation and gimbal motors were set to an angular velocity of 400° s^{-1}, providing a nominal torque of 4.46 Nm. Torques were generated in both directions about the roll, pitch, and yaw axes (see Figure 5.1). Results of the investigation are shown in Figure 5.2.

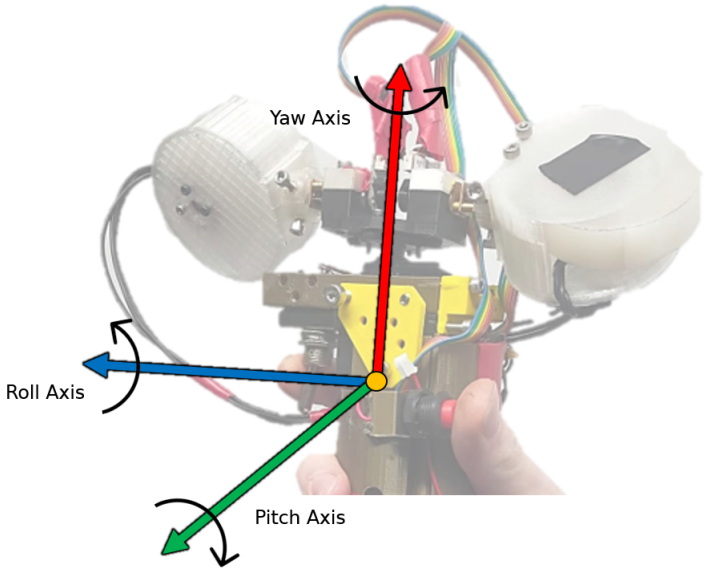

Figure 5.1: Roll, pitch, and yaw axes.

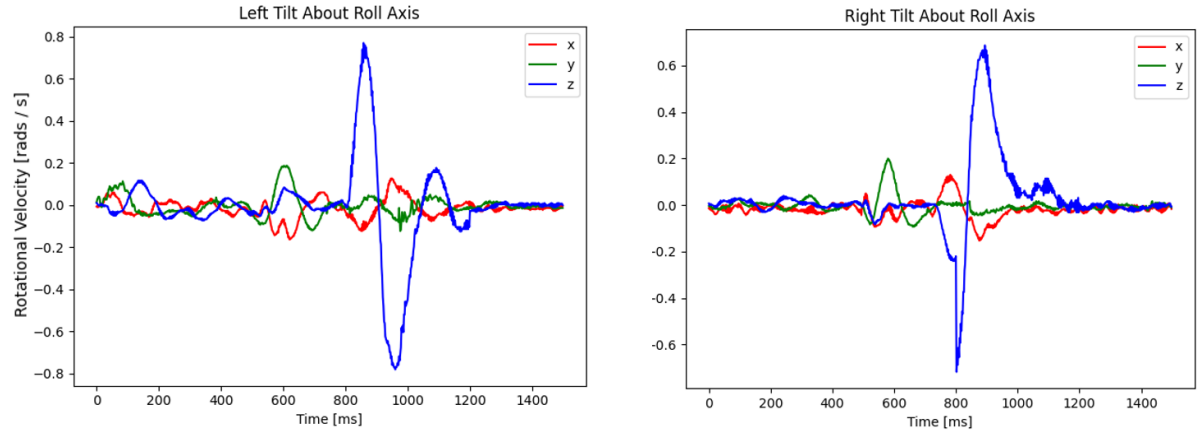

(a) Roll axis

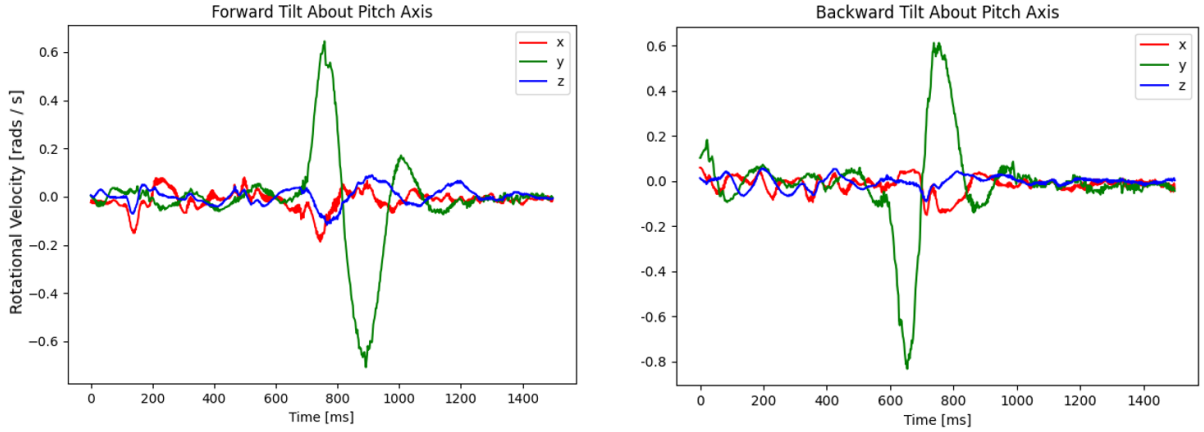

(b) Pitch axis

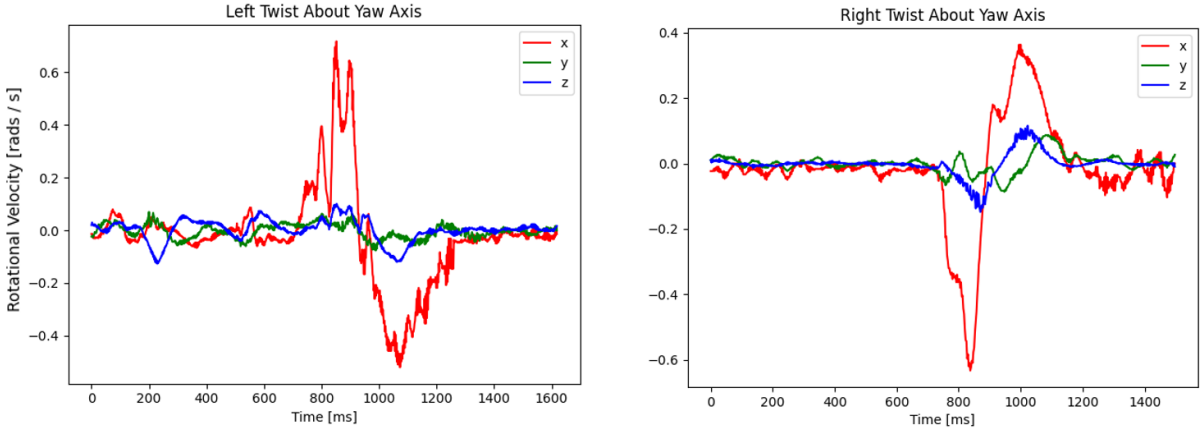

(c) Yaw axis

Figure 5.2: Angular velocity of the Gimbalscope during haptic cues about the roll, pitch, and yaw axes over 1400ms.

Considering angular velocity as an analogue to torque, it is evident that the Gimbalscope succeeds in its ability to isolate moments to a single axis. The peaks and troughs of the graphs in Figure 5.2 show this clearly, with all six haptic cues about the three axes producing the expected initial direction of rotation. The peak magnitude of each cue's rotational velocity is broadly similar to all others, ranging between 0.6 $rads^{-1}$ and 0.8 $rads^{-1}$. A level of background noise is evident about each axis during haptic cues. This is because the Gimbalscope was held by hand since no appropriate three-axis rig was available.

I discovered a large reactionary torque that occurs after each cue. The torque was felt by participants during experiments, but its existence is verified by the graphs in Figure 5.2. After each initial peak/trough of angular velocity (the intended cue direction), there appears to be an approximately equal and opposite rotation. This is not accounted for in the equations of section 2.2.1. The reactionary torque is due to the gimbal motors' sudden stop as they approach their target orientation at the end of each cue. This causes the Gimbalscope to spring back to its initial orientation. My experiments have not determined whether this reactionary torque is undesirable to users. Even with the existence of this force, my experiments have shown that participants can reliably interpret the direction of cues and use them to successfully navigate towards target bearings (see section 5.2). Despite this, it would be possible to minimise the magnitude of the reaction. The PI controller responsible for governing flywheel gimbal behaviour could be adjusted to reduce the target angular velocity as gimbals approach their target orientation. Another solution would be to instead implement a PD controller with the objective of minimising negative angular jerk.

It can be seen in Figure 5.2c that torque induced about the yaw axis is not smooth - evident due to fluctuations in the x measurement. Torque magnitude does not appear to progress monotonically before and after reaching its peak value. In the hands of a user, this results in a subtle but noticeable jitter throughout yaw-isolated haptic cues. Moments about the yaw axis rotate in the same plane as the central gimbal servo. The fluctuations in the x-axis are caused by the gimbal servo being activated and braced. The servo attempts to remain stationary and resists torque about its axis of rotation. In doing so, it generates a greater opposing torque. Due to the resolution of the servo's potentiometer, this opposing torque is only induced after the servo's shaft has been rotated beyond a threshold, causing servo behaviour similar to that exhibited by a bang-bang controller. This cannot be avoided without replacing the servo, as the servo must be braced to keep the cue isolated to a single axis during the movement,

5.1.2 Vibration Profile Investigation

I found controlling vibrations induced by the Gimbalscope's flywheels to be a bigger factor in this project than first anticipated. Large, high-frequency vibrations are unpleasant for the user. The mechanical integrity of the Gimbalscope can be compromised when the device vibrates too much, occasionally causing the gimbals' shaft couplers to detach and grub screws to become undone. Furthermore, it is discussed in section 5.2.1 how large vibrations cause participants to grip the Gimbalscope more tightly, limiting the clarity of haptic cues. As such, I used the Mechanical Analysis Module to profile the vibration characteristics of the Gimbalscope over the full range of flywheel saturation, with the aim of using the data gathered to minimise vibration.

I performed two investigations. The first investigation aimed to describe the vibration characteristics of the Gimbalscope over a single spin-up from 0% to 100% flywheel saturation, plotting results in the time and frequency domains. The second investigation aimed to describe vibration characteristics over an aggregated set of readings, plotting results as a function of saturation. The methods and results of the two investigations are described in the subsequent subsections, followed by a discussion of the results.

Single Spin-up Vibration Characteristics

I secured the mechanical analysis module to the Gimbalscope and placed it on a flat tabletop. I calibrated the module while the flywheels were stationary. Once calibrated, I sent a command to the Gimbalscope to uniformly increase flywheel saturation from 0% to 100% over the course of 60 seconds. Timestamped three-axis acceleration data was sent to a PC via serial at 28800 bauds and logged using a Python script. It should be noted that acceleration data pertains to **linear** acceleration, not angular acceleration.

I used matplotlib to produce three plots, displayed in Figure 5.3. Subfigure 5.3a depicts the raw logged vibration data. Subfigure 5.3b illustrates the absolute derivative of the previous plot, depicting the magnitude of the rate of change of vibration acceleration. I performed a Fourier transform on the logged data, producing a plot of normalised acceleration in the frequency domain, displayed in Subfigure 5.3c.

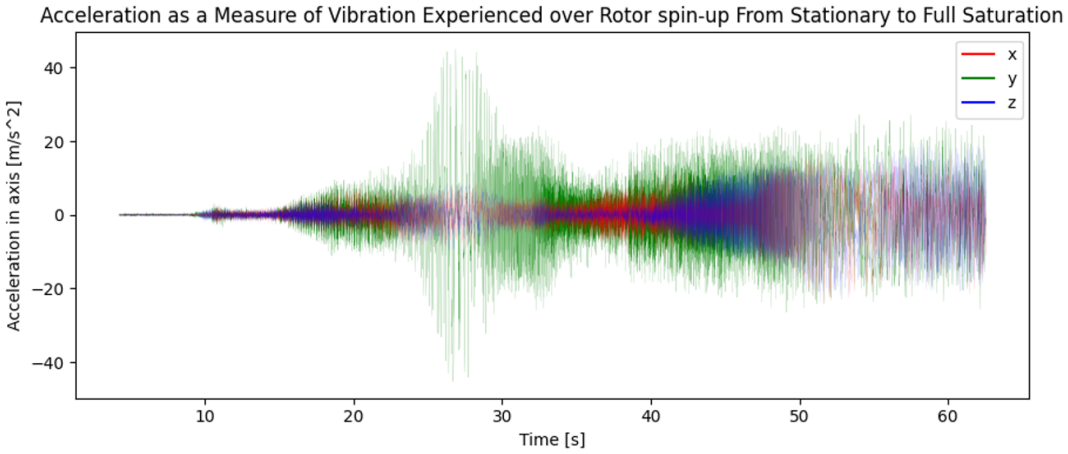

(a) Instantaneous Vibration Acceleration over Time.

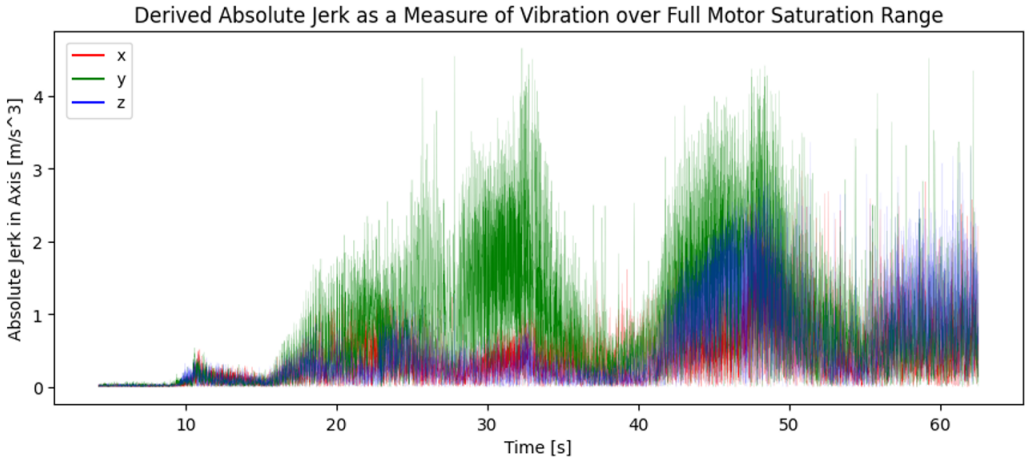

(b) Absolute Rate of Change of Acceleration over Time.

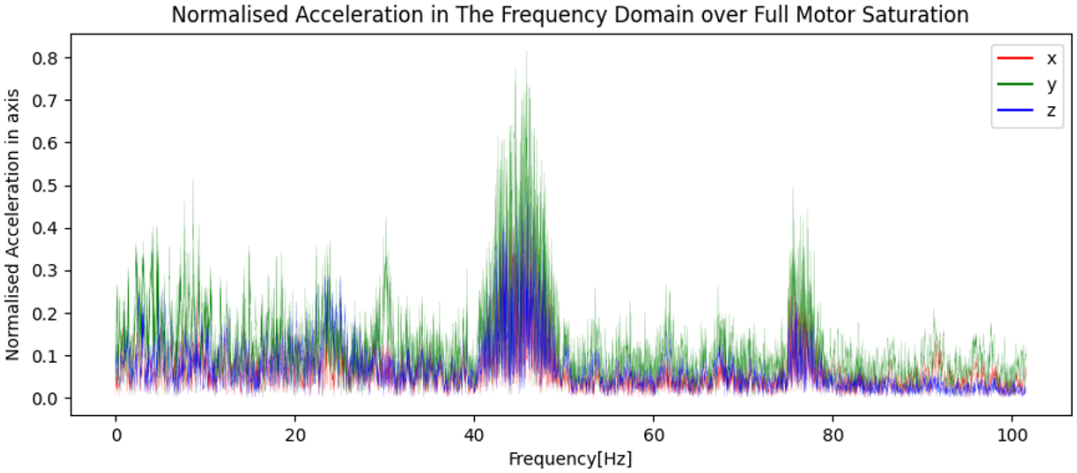

(c) Fourier Transform of Spin-up Vibration Profile.

Figure 5.3: Vibration profiles of the Gimbalscope sampled over flywheel spin-up from 0% to 100% saturation over 60 seconds.

Aggregated Saturation Vibration Characteristics

The graphs produced by the single spin-up investigation are not created from a large enough dataset to confidently isolate nodes of low vibration as a function of flywheel saturation. As a result, I conducted an aggregated vibration investigation to plot data at known saturation values.

I used the mechanical analysis module to gather 50 samples of 5 seconds duration, taken in discrete 2% increments from 0% to 100% saturation. Timestamped data was sent to a PC via serial at 28800 bauds and logged using Python. Samples were gathered in groups of 10. Before sampling each group, I calibrated the module at 0% flywheel saturation and then brought the motor to the appropriate speed before logging data. Exactly 5 seconds of data is logged before the module ceases recording and flywheel saturation is increased by 2%.

I used matplotlib to produce two plots, displayed in Figure 5.4. Subfigure 5.4a is composed of the waveform of 50 sample vibrations, ordered by saturation. Subfigure 5.4b shows the distribution of vibrations over saturation increments. The distribution of readings is displayed using a median line graph with shaded inter-quartile ranges.

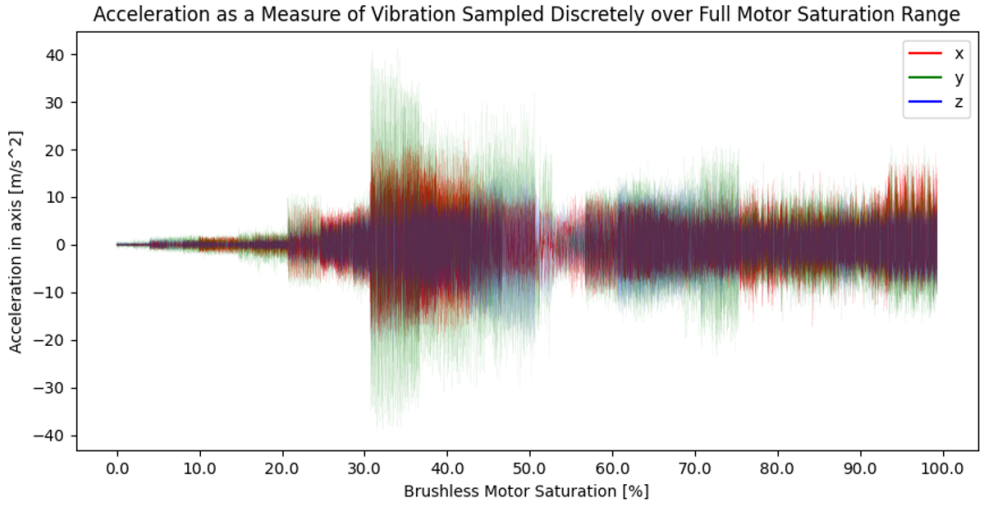

(a) Instantaneous vibration acceleration as a function of flywheel saturation.

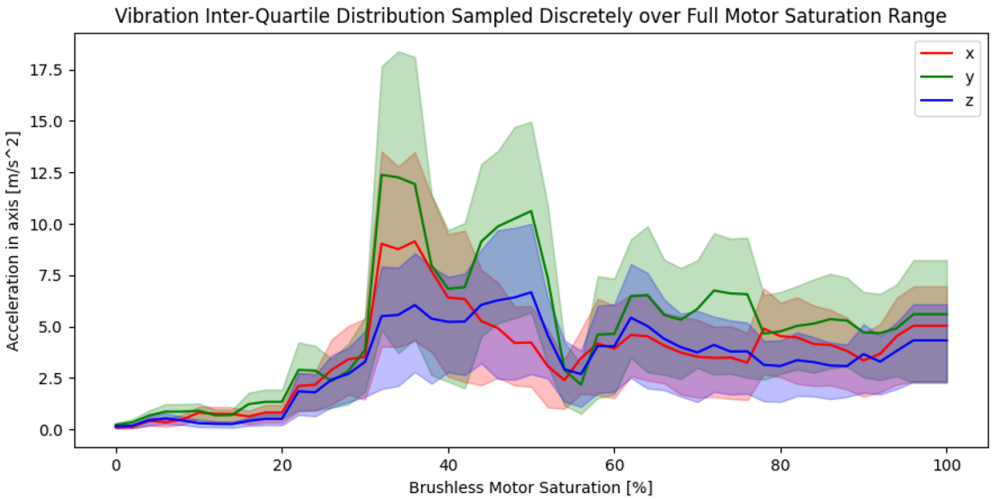

(b) Median and Inter-Quartile Vibration Distribution as a Function of Flywheel Saturation.

Figure 5.4: Aggregated vibration profile of the Gimbalscope over 50 independent trials, ranging from 0% to 100% flywheel saturation.

Discussion of Vibration Profiles

It is evident in both the single spin-up and aggregated sample profiles depicted in Figures 5.3 and 5.4 that vibrations in the lateral y-axis appear to be more prevalent than forward and vertical vibrations. Both figures show large vibrations at $\sim$ 30% flywheel saturation/$\sim$ 27s through spin-up. This could indicate the existence of a resonant frequency. This is supported by the Fourier transform plot in Subfigure 5.3c, which indicates a substantial increase in vibration acceleration magnitude at $\sim$ 45Hz. Subfigure 5.3b depicts a high average jerk magnitude surrounding this point, showing that the Gimbalscope is almost always experiencing a direction change in its vibration about this saturation. The existence of this potential resonant frequency is supported by the qualitative results of the torque perception test described in section 5.2.1. Participants described cues at 30% saturation as uncomfortable and tended to hold the device with a tighter grip.

Compared to the rest of the profile, vibrations below 20% flywheel saturation appear universally small. This can be felt while holding the Gimbalscope. This informed the saturation range for the threshold of discrimination experiment. Furthermore, there exists a relative node of vibration at 53% saturation, evident by its low amplitude in Subfigure 5.4a and low interquartile deviation in Subfigure 5.4b. This flywheel saturation provides an advantageous balance of torque and vibration. As such, this node was used to generate large haptic cue torques in the target identification experiment while keeping vibration comparatively low.

The prevalence of lateral vibrations in the y-axis may have been caused by an experimental bias. When each vibration sample was taken, the central gimbal servo was at its default position. As a result, the DCMG was positioned laterally in all trials, with its flywheels being located on the left and right of the Gimbalscope. As a result, there may be an over-representation of lateral vibration in the vibration profiles. To verify whether this is the case, it would be possible to take multiple vibration samples at perpendicular gimbal servo orientations and collate the resulting data. A statistical t-test could be performed between the readings of the most significant axis for each orthogonal DCMG orientation to determine if there exists a statistically significant difference in vibrations.

A critical limitation of the mechanical analysis module is its 300Hz maximum sample rate. It is possible that, for the purposes of describing the vibrations of the Gimbalscope, the module's Nyquist rate is too low and thus causes signal aliasing due to undersampling. In such a situation, the module misidentifies the vibration frequency, producing an inaccurate waveform. The ability of the mechanical analysis module to operate at high frequencies should be verified by an appropriate known device, such as a laser Doppler vibrometer.

5.2 User Evaluation

I performed three user experiments. Quantitative data was logged by the Unity control environment. Logged data was saved in JSON format. This enabled me to perform a large number of experiments and process the results at a later date. The large quantity of numerical data allowed me to perform statistical tests on the results. Data analysis was performed in Python using numPy and SciPy.

5.2.1 User Study I: Torque Perception Experiment

The torque perception experiment described in section 4.1 was the first experiment I performed. It measured torque direction identification rates across multiple flywheel saturations and torque directions from a set of 8 participants, totalling 288 trials. The results of the experiment are shown in Tables 5.1 and 5.2.

	Flywheel Saturation / Torque Magnitude		
	20% / 4.46 Nm	30% / 6.69 Nm	40% / 8.92 Nm
Identification Rate	0.962	0.988	0.987

Table 5.1: Torque perception test Identification Rates by Torque Magnitude.

	Cue Direction					
	Forward Tilt	Backward Tilt	Left Tilt	Right Tilt	Left Twist	Right Twist
Identification Rate	1.000	1.000	1.000	0.944	0.928	1.000

Table 5.2: Torque perception test Identification Rates by Cue Direction

The mean identification rate in the study was 97.9%. Participants made few mistakes in identifying distinct orthogonal cues. Incorrect answers were given in only six of the 288 trials, with some participants incorrectly identifying right tilts (clockwise roll) and left twists (counter-clockwise yaw).

Since the measured outcome data is binary (success or failure to identify), I organised the results into contingency tables. A pair of chi-squared tests yielded no statistically significant difference in results over flywheel saturations and cue directions, yielding chi-squared and p-value pairs of ($F = 1.72$, $p = 0.423$) and ($F = 10.97$, $p = 0.052$) respectively.

Quantitivate Discussion

The results of the torque perception experiment confer with the results of JM Walker's similar identification study, which achieved a success rate of 99.3% (compared to 97.9%). This similarity can be said with near statistical certainty. With the Gimbalscope, users were able to distinguish the six directions in this study almost perfectly.

The lack of a statistically significant relationship between flywheel saturation and identification rate suggests that increasing peak cue torque beyond 4.46 Nm has no bearing on user identification. Furthermore, the lack of significant difference between cue directions suggests participants are equally able to identify cue orientations. The similarity between identification rates per flywheel saturation motivated further investigation, leading me to design the threshold of discrimination experiment.

Qualitative Discussion

I maintained a dialogue with participants throughout the experiment to understand the language humans use to describe the motion of the Gimbalscope. most participants were not natively familiar to the terms *roll*, *pitch*, and *yaw* to describe axes of rotation. As such, these participants employed an inconsistent range of terms to describe rotations. This prompted me to ask participants for clarification on their answers by asking them to gesture the cue direction, increasing the time taken to process each participant. Eventually, these participants tended to settle on their own consistent terms to describe cues. Terms included 'to me' and 'away', as well as 'to that side' while pointing in a direction.

Participants familiar with joysticks were able to natively understand *roll*, *pitch*, and *yaw*. Analogies were made to flight simulators, with participants describing 'pitch-up', 'pitch-down', 'roll-clockwise', and 'roll-counter-clockwise' to correctly identify torque directions.

Participants reported gripping the device tighter at high motor saturation due to the vibration of the device. A tighter grip makes the device rotate less during haptic cues, reducing the apparent strength of cues.

5.2.2 User Study II: Threshold of Discrimination Experiment

The threshold of discrimination test described in section 4.2 was the second experiment I performed. It measured torque identification rates and the number of haptic cues required to identify a given torque, across multiple flywheel saturations and torque directions. 13 participants took part in the study, totalling 624 trials. The results are shown in Tables 5.3 and 5.4. I removed the results of two anonymous participants from the study after they disclosed a diagnosis of dyspraxia to me after the experiment, the implications of which are discussed later.

Results

	Flywheel Saturation / Torque Magnitude			
	5% / 1.12 Nm	10% / 2.23 Nm	15% / 3.35 Nm	20% / 4.46 Nm
Identification Rate	0.574	0.904	0.972	0.974
Mean Cues Requested	3.010	1.748	1.524	1.293

Table 5.3: Threshold of discrimination test identification rates and mean cues requested by torque magnitude.

	Cue Direction					
	Forward Tilt	Backward Tilt	Left Tilt	Right Tilt	Left Twist	Right Twist
Identification Rate	0.866	0.838	0.842	0.844	0.888	0.859
Mean Cues Requested	1.890	1.898	1.895	1.893	1.889	1.899

Table 5.4: Threshold of discrimination test identification rates by cue direction.

The mean identification rate in the study was 85.6%. In Table 5.3, a monotonic relationship exists between flywheel saturation and identification rate, as well as the average number of haptic cues requested. Participants gave the most incorrect answers at 5% saturation, however, the 57% success rate is still far above the random expected value of 16%.

I organised identification rates and flywheel saturations into contingency tables. Over **all** saturations, a chi-squared independence test yielded a statistically significant result ($F = 130.05$, $p = 5.29 \times 10^{-28}$). Since p is far less than 0.05, the test strongly indicates that at least one set of results deviated from the others due to cue magnitude. To investigate this further, I removed the most different set of results (5% saturation) from the contingency table and calculated the chi-squared values for **10%**, **15%**, and **20%** saturation to test for independence. These results also indicated the existence of one or more statistically independent sets of results ($F = 9.51$, $p = 8.60 \times 10^{-3}$). Since the previous chi-squared values resulted in statistical significance, I removed the set of results pertaining to 10% saturation from the contingency table and calculated the values for **15%** and **20%** saturation ($F = 0.108$, $p = 0.742$). These values indicate statistical similarity between the two sets of results.

To investigate the statistical significance of the correlation between flywheel saturation and the mean cues requested by participants, I performed a Kruskal-Wallis test ($F = 172.26$, $p = 4.13 \times 10^{-37}$), the results of which heavily imply this correlation is not to chance. The correlation and distribution of cues are presented as a violin plot in Figure 5.5.

I performed a chi-squared test over cue directions and identification rates ($F = 1.42$, $p = 0.92$), the results of which strongly indicated no relationship between the two variables.

The success rate of participants identifying haptic cues at 20% saturation confers with that of the torque perception experiment (97.4% compared to 96.2%), grounding the results of the threshold of discrimination test in the context of the previous study.

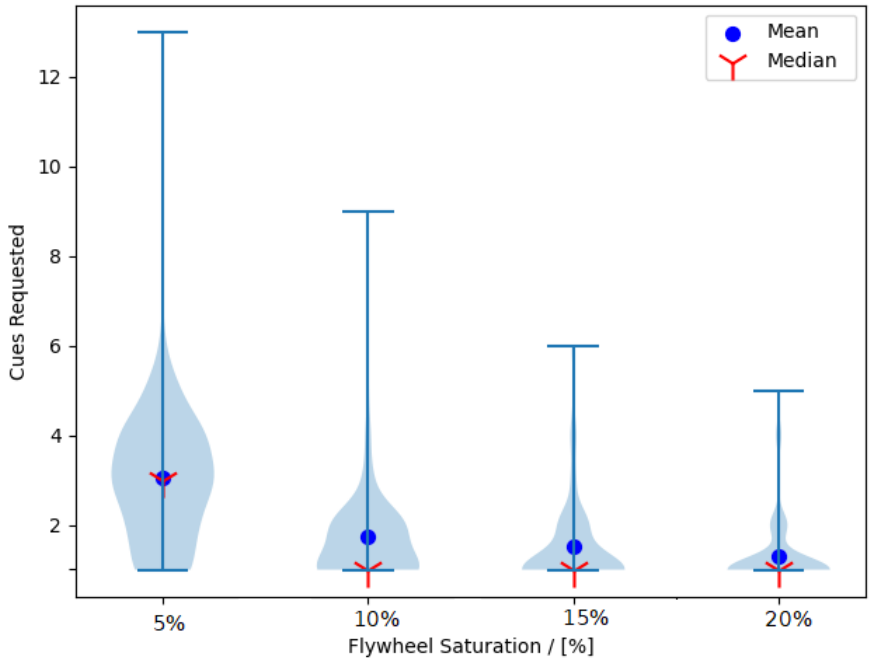

Figure 5.5: Violin plot of the number of cues requested by participants over motor saturations.

Quantitative Discussion

We can infer from the results of the threshold of discrimination test that there exists a saturation value between 10% and 15%, below which starts to cause a statistically significant drop in cue identification rates, as demonstrated by the chi-squared tests in the previous subsection. The most significant drop in cue perception occurs between 10% and 5% flywheel saturation. We can also state that there is no significant difference in identification rates between 15% and 20% saturation. However, on average, participants required more haptic cues to be certain of their answer when presented with cues of 15% saturation compared to 20%. This relationship holds across the experiment, with a negative correlation between flywheel saturation and the number of haptic cues required.

Some participants required significantly more attempts to identify cues. This is most evident at lower flywheel saturations, seen in Figure 5.5. All the distributions are positively skewed, with mean results greater than median results. This suggests that there exists a proportion of participants who are either less haptically perceptive than others, or seek to be more certain of their answers. The decreasing distribution of results for each flywheel saturation implies participants were more certain of their answer with a greater haptic cue torque magnitude. This information was not captured in the previous study.

The study was unable to find the threshold at which participants were unable to perceive cue direction - i.e no statistically significant dissimilarity between results and a random sample of answers. This threshold could be explored by designing a further study in which motor saturation is slowly decreased per trial, with participants required to identify cues of ever-decreasing magnitude.

Qualitative Discussion

There exists a potential systemic bias in the design of the study. I asked participants to sit in the most optimal position to feel the effect of haptic cues (as in Figure 4.1), i.e with a loose kinematic chain to allow their wrist to move more freely. As such, identification rates may be lower if I asked participants to sit or stand in different positions.

I had to remove the results of two participants who disclosed a diagnosis of dyspraxia due to not having the ethical clearance to gather data on vulnerable groups (including populations with a disability). This probes additional questions about the composition of cohorts in this study and other haptic studies. I do not know whether other participants in my cohort have similar diagnoses, since both participants voluntarily self-disclosed their condition unprompted. There may be many other factors that influence

a participant's ability to perceive haptic cues that were not previously considered, such as arthritis or blood pressure. This stresses a point about accessibility considerations of haptic device research and how we should consider designing for an inclusive audience.

Overall, the Gimbalscope performed strongly in this study, motivating further investigation with a use-case in the target identification experiment.

5.2.3 User Study III: Target Identification Experiment

The target identification experiment described in section 4.3 was the third and final experiment I performed. It aimed to quantitatively explore how participants use the Gimbalscope as a navigation aid in a two-degrees-of-freedom environment. 6 participants were tasked with locating a set of 7 target bearings, located at 045°, 090°, 135°, 180°, 215°, 270°, and 315° to the participant's start orientation, totalling 42 trials.

For each trial, the Gimbalscope's onboard three-axis gyro tracked the participant's orientation over time, plotting its path inside a 3D sphere (see Figure 5.6). Paths are drawn by two representations: stream and keyframe. Stream representations (displayed on the left of Figure 5.6) take the 5Hz continuous orientation telemetry of the Gimbalscope, spherically interpolate between each point, and plot a smooth path trace on the inner surface of the sphere. Keyframe representations (displayed on the right of Figure 5.6) use orientation telemetry at points at which participants request haptic cues. Straight lines are plotted within the interior of the sphere between points on its surface, visualising the path of participants as a series of jumps. Final path destinations are marked with a coloured pin. Note that there exists a discrepancy in pin positions between stream and keyframe visualisations. This is because stream visualisation draws the orientation path up until the participant confirms their target, whereas the keyframe visualisation only draws up until the last haptic cue, which is before target confirmation.

Results are summarised in Table 5.5.

Results

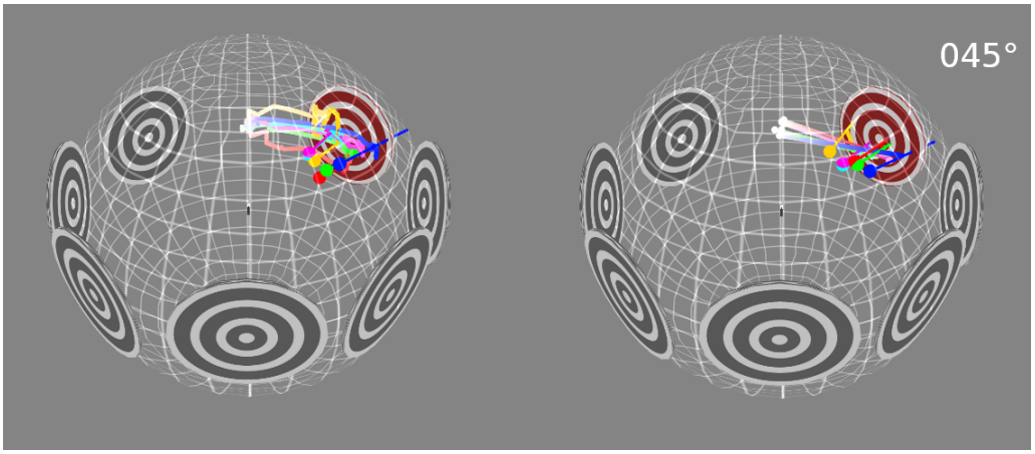

(a) Paths taken by participants to orientate towards bearing 045°.

Figure 5.6: Continuous (left) and keyframe (right) paths taken by participants to orientate towards a target bearing during the target identification test.

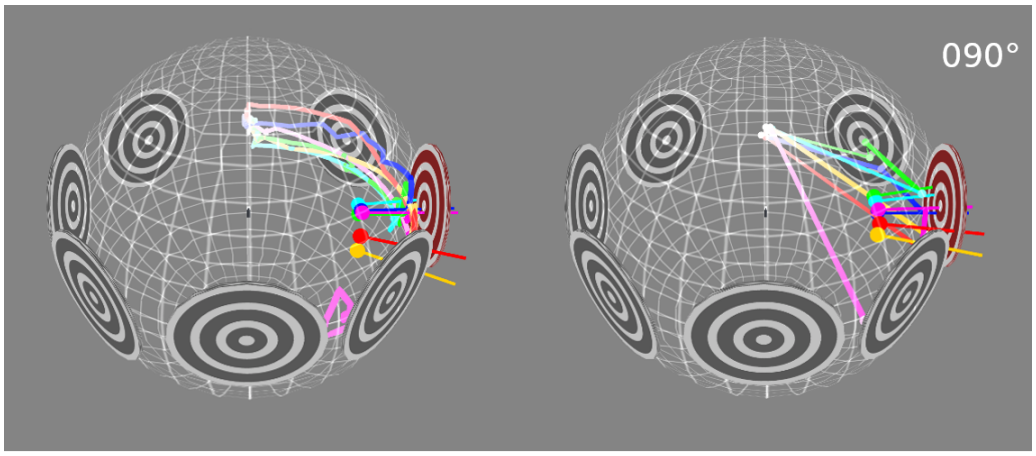

(b) Paths taken by participants to orientate towards bearing 090°.

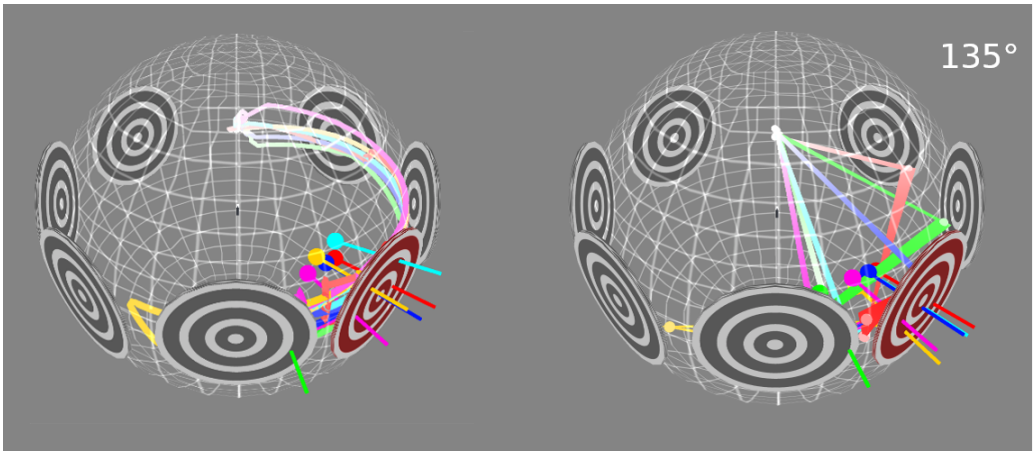

(c) Paths taken by participants to orientate towards bearing 135°.

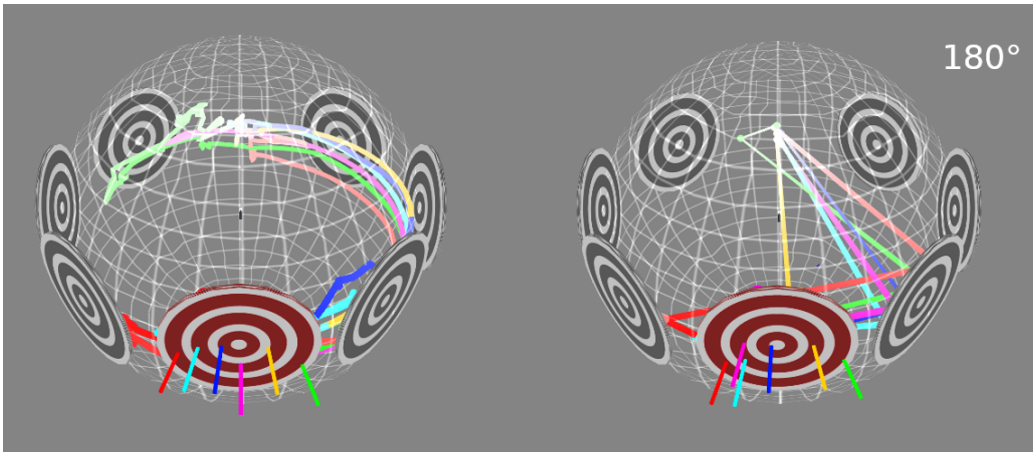

(d) Paths taken by participants to orientate towards bearing 180°.

Figure 5.6: Continuous (left) and keyframe (right) paths taken by participants to orientate towards a target bearing during the target identification test (cont.).

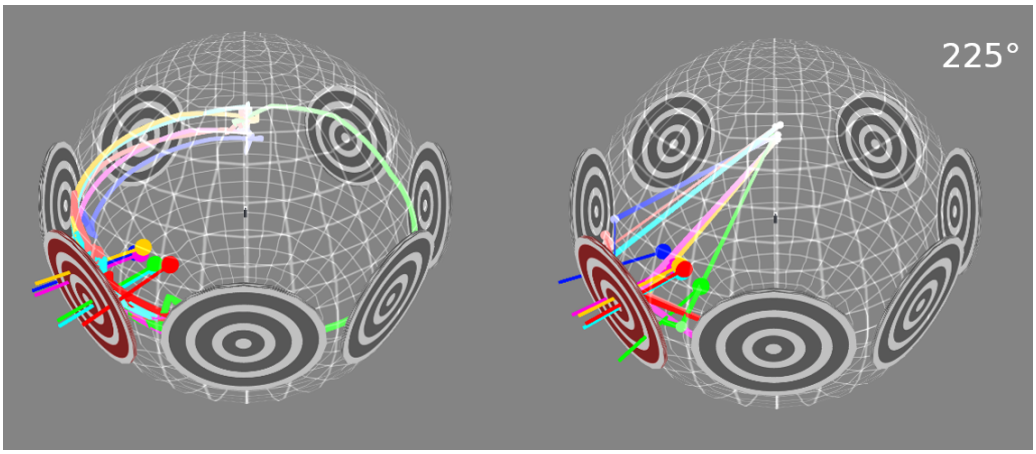

(e) Paths taken by participants to orientate towards bearing 225°.

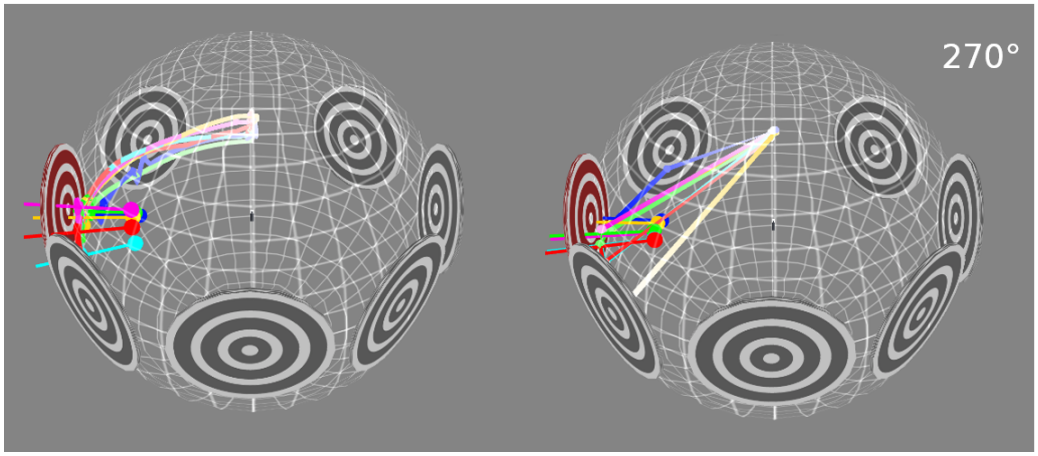

(f) Paths taken by participants to orientate towards bearing 270°.

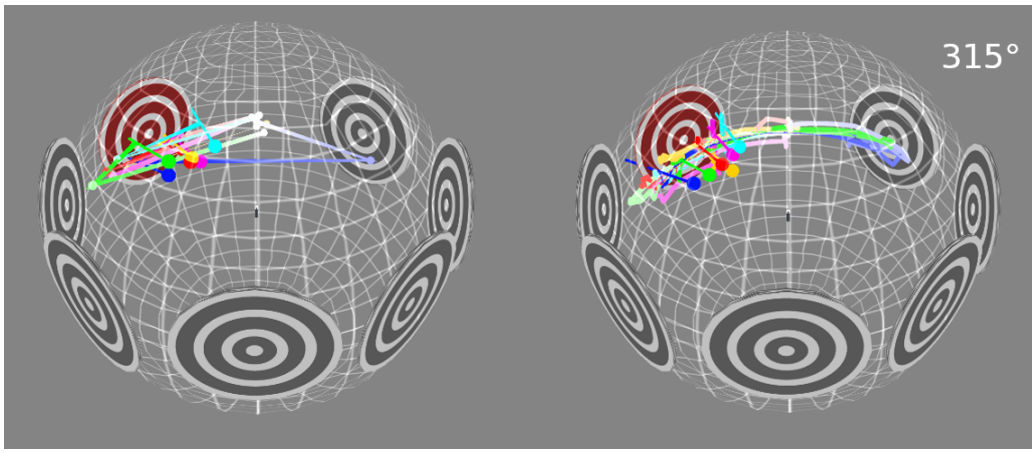

(g) Paths taken by participants to orientate towards bearing 315°.

Figure 5.6: Continuous (left) and keyframe (right) paths taken by participants to orientate towards a target bearing during the target identification test (cont.).

	Target Bearing						
	045	090	135	180	225	270	315
Identification Rate	1.00	1.00	0.86	1.00	1.00	1.00	1.00
Time Taken [s]	23.4	28.7	32.2	36.3	37.6	23.3	34.6
Cues Requested	2.83	4.00	5.33	4.17	5.00	3.67	3.83

Table 5.5: Mean target identification test results averaged over participants.

Discussion

The identification rate for all bearings, aside from 135°, is 100%, giving an overall identification rate of 97.62%. This indicates that almost all participants were able to successfully orient themselves towards and identify target bearings with the aid of the Gimbalscope. On average, participants took 30.1 seconds and 4 haptic cues to identify each target (rounded to the nearest integer). Bearings opposite to the participant's starting orientation required more haptic cues and took longer to identify. However, the dataset is not large enough to make any statistical claim.

Participants tended to orientate towards the target orientation taking the path of the shortest angle, except for one outlying case at 225° (see Subfigure 5.6e). Participants could reliably use directional cues to make large changes in their orientation, evidenced by large jumps from the start orientation in the keyframe plots. The majority of haptic cues were requested within 90° of the target bearing as participants honed in on their selection with small adjustments.

Participants experienced difficulty correctly responding to small orientation adjustments. This resulted in a participant misidentifying a target at 135° (see Subfigure 5.6c). There exist multiple factors which may be contributing to this difficulty. Firstly, experimental research suggests that the threshold angle at which a human is able to differentiate forces is approximately 15° [9]. Secondly, some participants had a tendency to tilt the device about the roll axis. Since this experiment did not track the roll axis, haptic cues could become distorted. Further factors may be due to the technical limitations of the Gimbalscope, discussed in the next subsection.

Discussion of Technical Limitations

The target identification experiment was more of a real-world use case for the Gimbalscope compared to the two previous studies. The experiment utilised more of the Gimbalscope's technical capabilities. As such, the device was tested more comprehensively than in previous studies as all components were required to function seamlessly. As a result, to create the target identification test, I had to make a set of design choices to mitigate some of Gimbalscope's technical limitations.

Firstly, participants were given an extended familiarisation period before performing the experiment. This was to learn how to correctly use the Gimbalscope in the context of the experiment's prodecures. I had to remind some participants to remain stationary mid-cue. This is because the DCMG must take time to arrange itself to a resolved orientation before delivering a cue. Torque orientation is resolved upon a cue request, rather than as a floating resolution estimation. Moving the device while the DCMG is arranging itself results in an incorrect torque vector.

Secondly, the target bearings to which participants were directed were not anchored to the physical world. Bearing were independent of targets in the testing room, aside from being used to reset and calibrate orientation. I designed the experiment so that this did not impact participants, who wear a sight-blocking welding mask during all trials. I designed the physical targets to prime participants as to the nature of the experiment using a familiar affordance. The targets also helped demonstrate to participants the relationship between the actual vs the estimated orientation seen in the Unity environment (as seen in Figure 4.2b). This design decision mitigated the drift inherent in the device's three-axis gyro. Combined with the participants' inability to visually anchor themselves, the independence of target bearings to any real-world orientation allowed the experiment to be performed within the Gimbalscope's estimated (potentially inaccurate) frame of reference. As such, it was impossible for the DCMG to deliver an incorrect cue direction as a result of gyro drift.

Thirdly, due to the manufacturer, the servo used as the Gimbalscope's central gimbal has a maximum traversal of 135°. I did not realise this until I designed the target identification experiment. As a result, there exist two blind spots of 45° in the horizontal plane in which the Gimbalscope is unable to direct a torque (see Figure 5.7). These blind spots added to the difficulty participants experienced in making

minor orientation adjustments. I hypothesise that this was the reason one participant failed to identify bearing 135°.

To compensate for the blind spots, if a haptic cue direction lies within either of Figure 5.7's unshaded areas, the direction is rounded to the nearest valid angle. This substantially reduces both precision and accuracy, but does allow for some form of haptic cue to be summoned. Rounding torque direction towards the forward vector can indicate a false positive cue, causing participants to misidentify a target bearing.

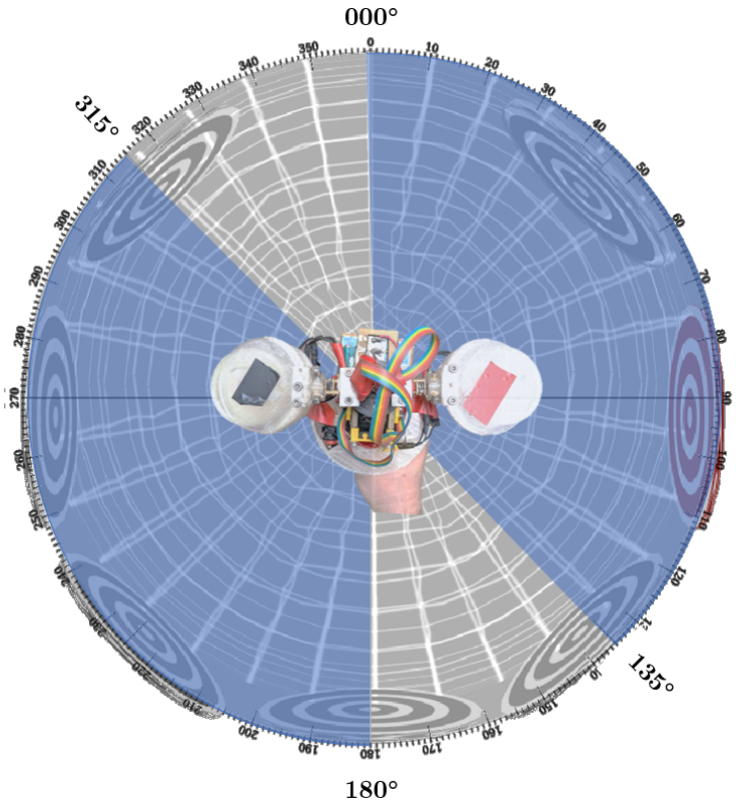

Figure 5.7: Gimbalscope torque direction blind spots in 2-DOF.

It was necessary to limit the pitch axis of the Gimbalscope's orientation estimation to ± 25° due to a disproportionate drift in the 3GD20H three-axis gyro's readings. The pitch axis of the gyroscope appeared to be especially susceptible to non-linear vertical drift while moving through space. As such, I was unable to calibrate against this effect. To mitigate the drift and allow for more comprehensive orientation tracking, the three-axis gyro could be replaced by a well-manufactured 9-DOF IMU, combining gyroscope, accelerometer, and magnetometer readings to produce a more accurate pose estimation.

5.3 Miscellaneous Evaluation

5.3.1 Evaluation of Gimbal Control

I found that my upper gimbal control system occasionally malfunctioned. These malfunctions would cause the gimbals to become out of sync (and thus produce ambiguous torques) or make multiple revolutions. This was an issue as it often required me to use the emergency stop button to prevent wires from tangling. While reducing non-interruptable tasks on the Arduino, such as serial read/write, has helped to mitigate this issue to some extent, it didn't completely solve the problem. A potential solution could be to implement a dedicated motor control board or use a more powerful Arduino to address this problem. Despite my efforts, I have not been able to fully diagnose the issue, however, I hypothesise the cause may be due to unreliable quadrature encoders.

5.3.2 Evaluation of Microcontrollers

The Gimbalscope's control loop could operate at a higher rate by using a more powerful board than the Arduino Mega, such as the Arduino Due with its 32-bit ARM core microcontroller. This would improve the Gimbalscope while still allowing the use of the same source code. The Due's additional interrupt pins would allow for closed-loop control of the central gimbal, allowing for the replacement of the servo with a motor and encoder. Alternatively, the onboard electronics could be simplified and completely overhauled by using an alternative board, such as a Raspberry Pi Pico. This is pertinent because the Gimbalscope's electronics are relatively heavy and bulky. Despite the increased power consumption, using a Pico would negate the need for a dedicated radio operator board. Furthermore, refactoring the electronics into a PCB could further improve the form factor of the project, making it even more compact and efficient.

5.3.3 Evaluation of Chassis

Based on my observations during experiments, I noticed that the handle of the Gimbalscope was too large for some participants' hands. While some participants were able to hold the trigger and momentary button simultaneously, others struggled to do so. This is due to a design bias on my part, as I have built the Gimbalscope to fit my own hand. As a result, some participants reported feeling uncomfortable holding the Gimbalscope, as if they were at risk of dropping it. Additionally, a few participants found it challenging to pull the trigger, which required me to manually send fire commands from the unity environment.

The Gimbalscope is balanced, with its centre of mass located in the middle of the handle and similar moments of inertia about the roll, pitch, and yaw axes. This means the rotation experienced by the device due to torques generated about the yaw axis is approximately equal in magnitude to that of the pitch and roll axes. This is reflected by Figure 5.1 in the mechanical analysis. This most likely contributed to the equal identification rates given by participants for each cue direction.

5.3.4 Evaluation of Inertia Calculation Software

The purpose of the inertia calculation software I produced using Python was to produce a low-precision estimate of the Gimbalscope's x, y, and z moments of inertia. The method I used assumes each of the three marked sections (see Figure 3.14) is of uniform density. The internal components are not modelled. Currently, the mass of sections is defined by sorting all points by their height (z) coordinate, then defining the required mass to which all points should sum between pairs of z values. This method does not allow for defining the density of volumes radial to the centre. To improve the accuracy of the inertial estimate, it should be made possible to place and define the density of individual components anywhere within the 3D volume. Despite this, the software helped ensure the creation of a balanced device, as well as justify flywheel specifications.

Chapter 6

Conclusion

6.1 Contributions and Achievements

This project has created a new proof-of-concept 3-DOF ungrounded haptic device for inducing directional force feedback using asymmetric pulses from a DCMG. According to Haptipedia [24], the Gimbalscope is the first untethered handheld device of its kind capable of 3-DOF.

I have investigated the performance of the Gimbalscope through three user experiments. In the torque perception experiment, I successfully reproduced the results of J M Walker's Direction Identification study with her tethered DCMG device [34]. Participants were able to distinguish the direction of haptic cues about the *roll*, *pitch*, and *yaw* axes in almost every trial with a mean 97.9% identification rate. I conducted the experiment over 20%, 30%, and 40% flywheel saturation and found no statistically significant difference in identification rate.

In the threshold of discrimination test, I established the existence of a statistically significant threshold of flywheel saturation between 10% and 15%, at which the ability of users to correctly perceive haptic cues begins to diminish. I measured the number of haptic cues participants required to identify the direction of a haptic cue, uncovering a statistically significant negative correlation between flywheel saturation and the number of cues required. I conducted the experiment over 5%, 10%, 15%, and 20% flywheel saturation.

In the target identification test I demonstrated that, in conjunction with orientation resolution, users can use the Gimbalscope's haptic cues in 2-DOF as a navigation aid to locate and identify target bearings in the horizontal plane with a near 100% success rate.

I have built a physical testing framework for the Gimbalscope with accessible components and software. I created low-cost alternative implementations of equipment where applicable, such as the Mechanical Analysis Module to stand in for a force/torque plate and vibrometer, as well as a finite element method implementation to estimate the angular inertia of 3D models. I used the Mechanical Analysis Module to prove that the Gimbalscope is able to isolate the torque of its haptic cues to a single axis, as well as profile the device's vibration while its flywheels are in motion.

6.2 Project Status

All of the aims listed in section 1.1 have been fulfilled. The completion of each aim is summarised and referenced using angle brackets: e.g. ⟨aim 1⟩.

I successfully created a scissored-pair Dual Control Moment Gyroscope and verified that it can isolate a torque to a single axis ⟨aim 1⟩. This is demonstrated both empirically with the Mechanical Analysis Module (see section 5.1.1) and in a human context with the Torque perception test (see section 5.2.1). The DCMG setup ensures the Gimbalscope is transparent in the hands of users.

The Gimbalscope uses a pair of 450mAh 3s LiPo batteries in parallel to provide power, removing the need for an external power supply ⟨aim 2⟩. This was safely achieved with fire-retardant insulation, overcurrent protection, voltage monitoring, and a 15A removable fuse (see section 3.1.1).

The Gimbalscope is controlled remotely using 900MHz digital radio, facilitated by a pair of Adafruit RFM69HCW Transceivers, as described in section 3.5 ⟨aim 3⟩. This was a functionally successful design choice, enabling duplex communication between the Gimbalscope and Unity control environment.

However, due to the rate at which the Arduino Micro radio operator can spool commands, there exists a noticeable delay of ∼500ms between command and actuation.

The Torque Perception and threshold of discrimination tests (sections 5.2.1 and 5.2.2) demonstrate that participants are able to reliably identify haptic cues in 3-DOF isolated about the *roll*, *pitch*, and *yaw* axes ⟨aim 4⟩ when flywheel saturation is above 15%.

Participants are able to use the Gimbalscope in a limited capacity as an orientation aid ⟨aim 5⟩, as demonstrated by the target identification test in 5.2.3. However, I do not believe that this capability has been comprehensively tested. Due to the pitch-drift issues of the 3GD20H three-axis gyro, I was only able to resolve orientations in 2-DOF in the horizontal plane. As such, I did not get the opportunity to evaluate the ability of participants to perceive 3-DOF torque vectors outside of isolation to the three primary axes.

With the exception of using Autodesk Fusion 360 to verify my CAD designs, the project exclusively used non-proprietary software and open-source components to contribute to the accessibility of research ⟨aim 6⟩. Arduino and Adafruit components are open-source and readily available off the shelf. The gimbal and flywheel motors are of standard specification and are mass-produced. Gimbal motors use standard 20D hall-effect magnetic encoders and brushless flywheel motors are controlled by open-source BLHeli_S ESCs.

6.3 Future Work

Gimbalscope Improvements

Future devices building upon the designs of Gimbalscope should seek to reduce vibration. I found this to be the biggest detraction from user experience. Structural 3D printed PLA components could be replaced with machined parts with finer tolerances, using a light metal such as aluminium. Flywheel axial wobble could be reduced by adding a support bearing to the top of the flywheel axis. Furthermore, form-factor optimisations could be made by replacing the PLA flywheels with smaller, denser, more radially distributed metal discs. Furthermore, a future model should include a central gimbal actuator capable of rotating through at least 180° to avoid torque blind spots.

As mentioned in section 5.3.2, form factor and performance improvements could be made by either replacing the Arduino Mega and Arduino Micro with the newer Arduino Due, or overhauling the device and utilising a Raspberry Pi Pico with inbuilt wireless network capabilities.

Future Research

Future research could expand upon the threshold of discrimination test by performing a just-noticeable-difference study, seeking to determine the minimum change in cue torque magnitude perceptible to humans. Furthermore, it could be worthwhile aiming to reproduce T. Endo's haptic angle perception research [9], which suggests the angle difference at which a human is able to differentiate forces is approximately 15°, using the Gimbalscope. Since T. Endo's study evaluates linear forces, not rotational torques, this could provide a basis for novel research.

If the onboard three-axis gyro's pitch drift issue is rectified, the target identification experiment could be expanded upon to include targets deviating from the horizontal plane, testing the Gimbalscope more comprehensively.

Onboard orientation tracking could be replaced with external 6-DOF pose estimation to accurately track both position and orientation. This could be used to evaluate participants in more detailed navigation experiments, such as mazes or environments including obstacles.

Finally, to reiterate section 1.2, a device similar to the Gimbalscope has the potential to provide feedback for object interactions and guidance within virtual environments. Such a device could help with pointing or aiming adjustments in alignment tasks with a controlled torque. This could have a potential military application in investigating the effect of haptic cues on weapon aim, or have a place in sports science studying racquet sports. Furthermore, it could enable portable guidance through large environments. This could prove useful in disability studies investigating pedestrian navigation, providing a different sensory modality from sight and sound.

Bibliography

[1] Drububu online voxelizer. Accessed: March 15, 2023. URL: https://drububu.com/miscellaneous/voxelizer/?out=obj.

[2] Faulhaber brushed geared, 0.97 w, 12 v dc, 100 mnm, 30 mnm, 151 rpm, 3mm shaft diameter. Accessed: April 3, 2023. URL: https://uk.rs-online.com/web/p/dc-motors/8734767.

[3] Moments of inertia in autocad. Accessed: March 29, 2023. URL: https://help.autodesk.com/view/AMECH_PP/2022/ENU/?guid=GUID-DF02CE27-4F3E-4AFE-B3D4-C483070E0B2A.

[4] Moments of inertia in fusion 360. Accessed: March 29, 2023. URL: https://forums.autodesk.com/t5/fusion-360-design-validate/properties-export-mass-moment-of-inertia-center-of-mass/td-p/10930372.

[5] T. Amemiya and T. Maeda. Asymmetric oscillation distorts the perceived heaviness of handheld objects. *IEEE Transactions on Haptics*, 1(9–18), 2008. doi:10.1109/TOH.2008.5.

[6] Michele Antolini, Monica Bordegoni, and Umberto Cugini. A haptic direction indicator using the gyro effect. In *2011 IEEE World Haptics Conference*, pages 251–256, 2011. doi:10.1109/WHC.2011.5945494.

[7] Akash Badshah, Sidhant Gupta, Daniel Morris, Shwetak Patel, and Desney Tan. Gyrotab: A handheld device that provides reactive torque feedback. In *Proceedings of the SIGCHI Conference on Human Factors in Computing Systems*, CHI '12, page 3153–3156, New York, NY, USA, 2012. Association for Computing Machinery. doi:10.1145/2207676.2208731.

[8] A Bicci. Analysis and design of an electromagnetic system for the characterization of magneto-rheological fluids for haptic interfaces. *IEEE*, 2005. doi:10.1109/TMAG.2005.846280.

[9] Takahiro Endo, Kanno Tomohiro, Kobayashi Mana, and Haruhisa Kawasaki. Human perception test of discontinuous force and a trial of skill transfer using a five-fingered haptic interface. *Journal of Robotics*, 2010, 01 2010. doi:10.1155/2010/542360.

[10] Canadian Centre for Occupational Health and Safety. How can one reduce the risk for work-related musculoskeletal disorders (wmsds) resulting from the use of hand tools? 2023.

[11] Anne Roudaut Gareth Barnaby. Mantis: A scalable, lightweight and accessible architecture to build multiform force feedback systems. *UIST '19: Proceedings of the 32nd Annual ACM Symposium on User Interface Software and Technology*, 2019. doi:10.1145/3332165.3347909.

[12] Hakan Gurocak, Sankar Jayaram, Benjamin Parrish, and Uma Jayaram. Weight sensation in virtual environments using a haptic device with air jets. *ASME Journal of Computing and Information Science in Engineering*, (130–135), 2013. doi:10.1115/1.1576808.

[13] Ravi Inampudi and John Gordeuk. Simulation of an electromechanical spin motor system of a control moment gyroscope. *AIAA Guidance, Navigation, and Control Conference*, 2022. doi:https://doi.org/10.2514/6.2016-0091.

[14] Brice Denoun Ata Otaran ivan Vitanov, Ildar Farkhatinov. A suite of robotic solutions for nuclear waste decommissioning. *MDPI*, 2021. doi:10.3390/robotics10040112.

[15] M. Aggravi N. Tsagarakis J. Bimbo, C. Pacchierotti and D. Prattichizzo. Teleoperation in cluttered environments using wearable haptic feedback. *IEEE*, 2017. doi:10.1109/IROS.2017.8206180.

[16] Brian Eberman J Radcliffe, Hong Z Tan. Human factors for the design of force-reflecting haptic interfaces. *Proceedings of the Third International Symposium on Haptic Interfaces for Virtual Environment and Teleoperator Systems - American Society of Mechanical Engineers*, 1994. URL: https://www.researchgate.net/publication/2269717_Human_Factors_For_The_Design_Of_Force-Reflecting_Haptic_Interfaces/stats.

[17] T. Mather J. Fiene K. N. Winfree, J. Gewirtz and K. J. Kuchenbecker. A high fidelity ungrounded torque feedback device: The itorqu 2.0,. *World Haptics 2009 - Third Joint EuroHaptics conference and Symposium on Haptic Interfaces for Virtual Environment and Teleoperator Systems, Salt Lake City*, 2009. doi:10.1109/WHC.2009.4810866.

[18] T. Mather J. Fiene K. N. Winfree, J. Gewirtz and K. J. Kuchenbecker. Control of a high fidelity ungrounded torque feedback device: The itorqu 2.1. *IEEE International Conference on Robotics and Automation, Anchorage*, 2010. doi:10.1109/ROBOT.2010.5509485.

[19] Fredrik Larsson, Petra Andersson, Per Blomqvist, and B.-E Mellander. Toxic fluoride gas emissions from lithium-ion battery fires. *Scientific Reports*, 7, 12 2017. doi:10.1038/s41598-017-09784-z.

[20] Martin Murer, Bernhard Maurer, Hermann Huber, Ilhan Aslan, and Manfred Tscheligi. Torquescreen: Actuated flywheels for ungrounded kinaesthetic feedback in handheld devices. *TEI '15: Proceedings of the Ninth International Conference on Tangible, Embedded, and Embodied Interaction*, 2015. doi:10.1145/2677199.2680579.

[21] Tal Oron-Gilad, Joshua L. Downs, Richard D. Gilson, and Peter A. Hancock. Vibrotactile guidance cues for target acquisition. *IEEE Transactions on Systems, Man, and Cybernetics, Part C (Applications and Reviews)*, 37(5):993–1004, 2007. doi:10.1109/TSMCC.2007.900646.

[22] Jingxian He Peiling Cui. Steering law for two parallel variable-speed-double-gimbal controlled moment gyros,. *ARC*, 2014. doi:10.2514/1.60403.

[23] Evren Samur. Performance measures for haptic interfaces. *Robotics Research: The Seventh International Symposium*, 1996. doi:10.1007/978-1-4471-4225-6.

[24] Hasti Seifi, Farimah Fazlollahi, Michael Oppermann, John Andrew Sastrillo, Jessica Ip, Ashutosh Agrawal, Gunhyuk Park, Katherine J. Kuchenbecker, and Karon E. MacLean. Haptipedia: Accelerating haptic device discovery. *Proceedings of the 2019 CHI Conference on Human Factors in Computing Systems*, 2019. doi:10.1145/3290605.3300788.

[25] P.C. Sen, C.S. Namuduri, and P.K. Nandam. Evolution of control techniques for industrial drives. In *Proceedings of International Conference on Power Electronics, Drives and Energy Systems for Industrial Growth*, volume 2, pages 869–875 vol.2, 1996. doi:10.1109/PEDES.1996.536387.

[26] Andreas S. Panayides Sotos Voskarides Cyril Novales Laurence Nouaille Constantinos S. Pattichis Pierre Vieyres Sotiris Avgousti, Eftychios G. Christoforou. Medical telerobotic systems: current status and future trends. *PubMed*, 2016. doi:10.1186/s12938-016-0217-7.

[27] Dollar AM Spiers AJ. Design and evaluation of shape-changing haptic interfaces for pedestrian navigation assistance. *IEEE*, 10:17–28, 2017. doi:10.1109/TOH.2016.2582481.

[28] Colin Swindells, Alex Unden, and Tao Sang. Torquebar. *Proceedings of the 5th international conference on Multimodal interfaces*, 2003. doi:10.1145/958432.958445.

[29] T.Smith. Creating greater vr immersion with tactile feedback. *Tactical Haptics*, 2020. URL: https://tacticalhaptics.com/files/IQT_Quarterly_Fall2014_Provancher.pdf.

[30] Jelle van Dijk, Remko van der Lugt, and Caroline Hummels. Beyond distributed representation: Embodied cognition design supporting socio-sensorimotor couplings. In *Proceedings of the 8th International Conference on Tangible, Embedded and Embodied Interaction*, TEI '14, page 181–188, New York, NY, USA, 2014. Association for Computing Machinery. doi:10.1145/2540930.2540934.

[31] Manuel Cruz-Hernandez Danny Grant Gabriel Robles-De-La-Torre Vincent Hayward, Oliver R. Astley. Haptic interfaces and devices. *Sensor Review*, 2004. doi:10.1108/02602280410515770.

[32] Ivan Vitanov, Ildar Farkhatdinov, Brice Denoun, Francesca Palermo, Ata Otaran, Joshua Brown, Bukeikhan Omarali, Taqi Abrar, Miles Hansard, Changjae Oh, Stefan Poslad, Chen Liu, Hareesh Godaba, Ketao Zhang, Lorenzo Jamone, and Kaspar Althoefer. Mobile torque display and haptic characteristics of human palm. *Proceedings of ICAT*, 2001. URL: https://www.researchgate.net/publication/238271619_Mobile_Torque_Display_and_Haptic_Characteristics_of_Human_Palm.

[33] Julie Walker. A dual-flywheel ungrounded haptic feedback system provides single-axis moment pulses for clear direction signals. *IEEE Haptics Symposium (HAPTICS), Philedelphia*, 2016. doi:10.1109/HAPTICS.2016.7463148.

[34] Julie Walker. Haptic orientation guidance using two parallel double-gimbal control moment gyroscopes. *IEEE*, 2018. doi:10.1109/TOH.2017.2713380.

[35] Andre Zenner and Antonio Kruger. Drag:on: A virtual reality controller providing haptic feedback based on drag and weight shift. *Proceedings of the 2019 CHI Conference on Human Factors in Computing Systems,*, 2019. doi:10.1145/3290605.3300441.